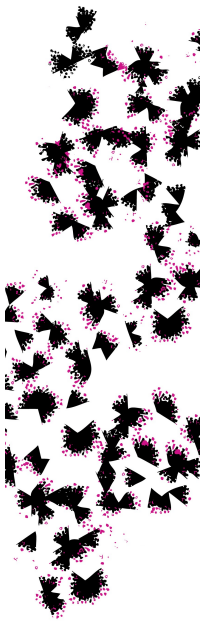

Self-powered Vibration Control using Piezoelectric Materials in High Precision Machines

S.A.A. (Samer) Abdelmoeti

MSc Report

Committee:
Dr.ir. T.J.A. de Vries
Dr.ir. J.F. Broenink
Dr.ir. J. Holterman
Ir. B. Jansen
Dr.ir. J. Van Dijk

August 2017

036RAM2017
Robotics and Mechatronics
EE-Math-CS
University of Twente
P.O. Box 217
7500 AE Enschede
The Netherlands

Preface

This is my master's graduation project in which I aim to bridge the gap between the practitioners and researchers in a specific research question with an industrial motivation. The topic combines my passion towards both mechanical vibrations and control theory, through an interesting physical phenomena which is piezoelectricity. In my opinion, piezoelectric or smart materials are quite underestimated in research. The main focus should not be only in developing smarter software, but also smarter hardware.

This project is a result of a collaboration between ASML and the Robotics & Mechatronics group at the University of Twente. The thesis is reported as a paper for submission to the "IEEE Transactions on Mechatronics". The research started as an investigation of incorporating piezoelectric materials for vibration damping of scanning blades within a lithography machine. During the literature review of the existing powered approaches, came up the practical limitation of the necessity of providing power to the piezoelectric versus powerless damping techniques. Hence, we initiated the research question of self-powered vibration control using piezoelectric materials for low level vibrations. Consequently, a research proposal based on a scanning motion energy harvester was suggested and agreed on. Accordingly, the problem was formulated, modelled, and identified. Afterwards, the appropriate solution was designed, implemented, and validated experimentally as discussed in the paper.

Firstly, I would like to acknowledge dr.ir. Theo de Vries for being my mentor before being my supervisor. Without his support and constant motivation I wouldn't have reached this point, I will always be thankful to him. I would like to thank ir. Bas Jansen for being unconditionally helpful, making the ultimate compromise between providing guidance and giving me research freedom. I also have to give the credit to Prof. Ayman El-Badawy, my undergraduate professor, for initiating my interest in these areas.

I would like to thank ASML, in particular the DUV optical column mechatronics group members and leader, ir. Jan Marius Schotsman, for providing the productive and friendly environment. I specifically thank Emile Demarteau for accommodating the NXT ReMa test-rig for my project.

I dedicate this to my family and friends.

Samer Abdelmoeti,
August 2017

Table of Contents

Introduction

In this work, a specific vibration control application within a high precision lithography machine is considered. Vibration control could be achieved by damping enhancement which is a typical approach for lightly damped structures. Damping could be introduced passively using tuned mass dampers or viscoelastic materials, however, volume and heat generation impose application limitations.

Piezoelectric materials are compact electromechanical transducers which can by actuation and sensing, or simply transduction, achieve vibration damping either through passive shunting or active feedback. Passive shunting typically require huge inductance values which can only be simulated using active circuits. This leads to the fact that both passive shunting and active feedback using piezoelectric materials require power for operation.

Implementing a powered damping approach in high precision machines is practically challenging in terms of connecting physical power wiring to each flexible structure. Therefore, overcoming power limitations is necessary for piezoelectric based damping to compete with other standalone damping approaches. There exist techniques in the literature for autonomous/self-powered damping using piezoelectric materials which utilize the vibration energy as a source of power. However, these are not feasible in high precision applications considering the limited energy of the nano/micro-meter scale vibrations. This work aims to achieve vibration damping of scanning blades within a lithography machine using embedded piezoelectric materials in a self-powered approach which is applicable to low level vibrations.

This report is structured as follows. The analysis, design, and results chapters are reported in the following research paper. Afterwards, the conclusion and recommendations are presented.

Self-powered Vibration Control using Piezoelectric Materials in High Precision Machines

Samer Abdelmoeti, Bas Jansen, and Theo de Vries

***Abstract*—In this paper, the vibrations of the reticle masking blades within a high precision lithography machine are considered. Vibration damping using piezoelectric materials is used as a suitable and compact concept for this application. However, the requirement of external powering in both passive and active damping using piezoelectric materials adds implementation constraints. A vibration control solution is proposed that is self-powered and not limited by the low-level vibrations. This is performed by energy harvesting utilizing the vibration excitation through the scanning motion. Experimental results validate the proposed approach for the blade excitation during normal operation.**

***Index Terms*—Vibration control, passive damping, active damping, piezoelectric materials, self-powered, autonomous, high precision, lithography machine.**

I. Introduction

VIBRATION control within high precision machines has been considered extensively in both literature and practice. The reason is that the performance of high precision machines is directly impacted by mechanical vibrations. Vibration control has been achieved through three main concepts: stiffness management, damping enhancement, and vibration isolation [1]. Primarily, design concepts are limited to stiffness management, i.e., maximizing stiffness and minimizing mass, due to the difficulties associated with introducing pure passive damping behavior. This generally lead to systems with lightly damped structures. This work investigates the introduction of passive or active damping in a specific high precision application while overcoming limiting implementation constraints in terms of external power requirements.

Photolithography machines are one example of high precision machines which are considered in this work. Particularly, the vibrations of the reticle masking blades during scanning motion within the lithography machine are addressed. Photolithography is the fundamental manufacturing process in the semiconductor industry. This process determines the final integrated circuits size, performance, and cost. Improving this process allows for more advanced technologies to be physically realizable and commercially available. The high precision process involves high accelerating moving parts which induce vibrations. Improving vibration control with the addition of damping enhances the overall performance of the lithography machine.

S. Abdelmoeti and T. de Vries are with the Faculty of Electrical Engineering, Mathematics and Computer Science, CTIT Institute, University of Twente, The Netherlands (emails: s.a.a.abdelmoeti@student.utwente.nl, t.j.a.devries@utwente.nl) .

B. Jansen is with the Department of Optical Column Mechatronics, ASML B.V., The Netherlands (email: bas.jansen@asml.com) .

Passive vibration damping is defined as introducing the damping behavior using passive elements which typically don't require external power. Alternatively, active damping is achieved by using actuators and sensors through a feedback control loop which mimics the damping behavior. This approach by definition utilizes power for producing the required control forces. Active damping provide improved performance versus passive approaches in addition to robustness.

Some passive vibration damping approaches such as tuned mass dampers are not compact enough with limited feasibility in a lithography machine. These are optimally located at the highest displacement of the vibrating structure. Viscoelastic materials on the other hand convert the vibration energy directly into heat at the location of the vibration. Heat generation at the critical parts is extremely significant for lithography machines which have the temperature tightly controlled. Additionally, these materials suffer from high outgassing [2], which might cause contamination of the lithography process.

On the other hand, there remains a challenging limiting factor for implementing active damping in high precision machines. This is the requirement of connecting physical power wiring from the highly accelerating flexible parts to the fixed world. For advanced lithography machines, this requires additional ambient to vacuum ports. Moreover, this becomes less practical when damping multiple structures.

Piezoelectric materials offer an interesting alternative solution for the introduction of both passive and active damping behaviors in high precision applications. These materials perform electromechanical transduction where damping can be achieved passively in the electrical domain. Moreover, piezoelectric elements can act as sensors and actuators in order to perform active damping. Piezoelectric transducers can be compactly embedded within the structure at the highest strain location instead of displacement. Furthermore, due to the fact that damping is introduced in the electrical domain, the heat generating element, i.e., resistor, can be located away from the temperature critical location.

Passive damping using piezoelectric materials is achieved by shunting the element with a resonant (RL) circuit [3]. In order to damp low frequency vibration modes this requires impractical high inductance values. These values cannot be realized physically using inductors, but rather synthesized virtually [4]. Therefore, active circuits such as simulated inductors, i.e., gyrators, are used in order to mimic the high inductance behavior [5], however require external power for operation. Nevertheless, the standard definition is to consider this approach as "Passive" since no power is supplied to the structure [4]. Hence, both passive and active damping using piezoelectric materials require power for operation.

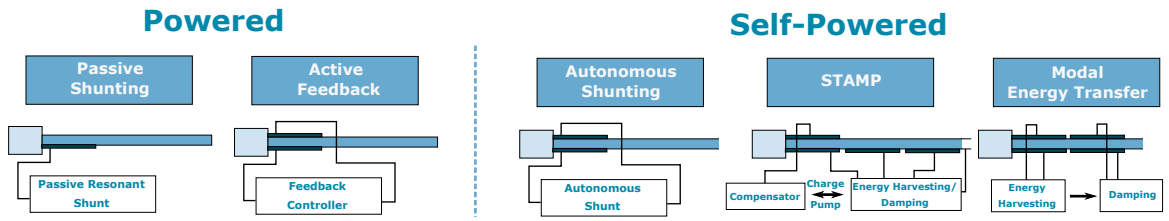

Fig. 1. Existing powered versus self-powered vibration damping solutions using piezoelectric materials. Self-powered techniques treat the beam vibrations as an energy source.

Different feedback controllers can robustly achieve active damping using collocated actuator/sensor piezoelectric pairs such as Direct Velocity Feedback (DVF) and Positive Position Feedback (PPF). Direct velocity feedback is unconditionally stable for all frequencies, given that perfect collocation is guaranteed [1]. The positive position feedback controller proposed by [6], introduces roll-off at high frequencies for robustness. For ultimate compactness, self-sensing approaches could be introduced in order to realize feedback control with a single piezo element as a self-sensing actuator [7].

Overcoming power limitations makes piezoelectric vibration damping more feasible and compete with other damping techniques, as an ultimately standalone solution. There exist solutions for self-powered techniques in the literature as shown in Fig.1. For example, autonomous shunting aims at designing shunt circuits which do not require power for operation. The idea is based on shunts which implement a switching law that allows for a physically realizable optimal value of L, much smaller than for a standard RL shunt [4]. However, the switch still requires power for operation that is provided using an additional signal from a sensing piezoelectric. The optimal switching laws and experimental results are discussed in detail in [8]. Performance achieved by autonomous shunting experimentally is half than that of standard resonant shunting. A "Strain Amplitude Minimization Patch" (STAMP) has been introduced as a self-powered discrete time piezoelectric vibration damper [9]. STAMP is a discrete time DVF which implements active damping. The concept is based on piezoelectric transducers which work both as power generators and actuators through adding a charge pump in between. When sufficient energy is accumulated the compensator and electronics are powered and the piezoelectrics act as actuators, otherwise they act as power harvesters to charge the pump, and so on, back and forth. Hence, this cycle is what makes the DVF a discrete time controller. Four piezoelectrics were used as power generators/actuators and a fifth piezo for sensing. Performance achieved was low when taking into account the number of piezos used [4]. Another self-powered vibration damping solution is proposed in [10], based on the idea of modal energy transfer. This aims at simultaneous harvesting and damping, but in contrast to STAMP, each with a different piezo. The idea behind modal energy transfer is to extract energy from some modes, in order to damp the targeted modes, thus achieve modal energy transfer.

However, in high precision applications the vibration deflections, which are in terms of micro/nanometer scale, have limited energy. This limited amount of vibration energy, which is still significant to the precision performance, is not enough to power the ciruitry proposed in the existing literature. In this work, a standalone system is proposed consisting of piezoelectrics and circuitry that is self-powered. The concept is to supply power from the source of vibration excitation, which is the scanning motion in this case, in order to damp the vibrations. By contrast, existing solutions consider the vibration itself as a source of energy. The principle of operation is to harvest energy using a piezoelectric film cantilevered in an orientation orthogonal to the high accelerating scanning motion. The harvested energy is utilized to power the vibration damping solution, which is either passive shunting or active feedback, using a piezoelectric patch embedded on the beam. An illustration of the proposed system is shown in Fig. 2. This concept could be generalized to harvest energy from one rigid body mode (scanning motion), in order to damp the complete system, i.e., 6 rigid body modes plus the flexible modes.

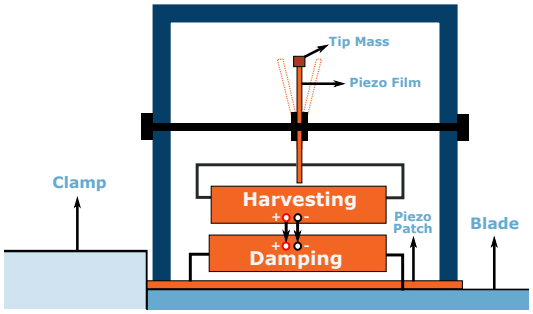

Fig. 2. Proposed concept of harvesting energy from the scanning motion using a cantilevered piezo film to power a vibration damping solution.

The paper is organized as follows. The problem of the reticle masking blade vibrations within the lithography machine is formulated in Section II. Section III presents the overall system modeling and identification. Additionally, the blade vibrations during typical operation are identified. Passive shunt and active feedback damping solutions using embedded piezoelectric elements are presented in Sections IV and V, respectively. Section VI proposes the self-powered vibration control solution using the piezoelectric energy harvester of scanning motion. Section VII shows the experimental results of the powered and self-powered vibration damping applied on the reticle masking test-rig. Conclusions are drawn in Section VIII.

II. Reticle Masking Unit Blade Vibrations

In this section, the problem of the reticle masking unit blade vibrations within a lithography machine is formulated.

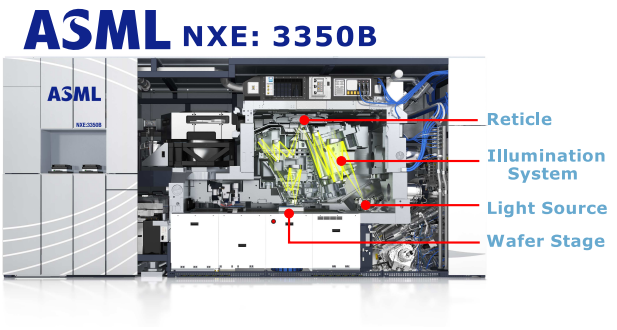

Fig. 3. Schematic of the latest lithography machine: ASML NXE:3350B [11].

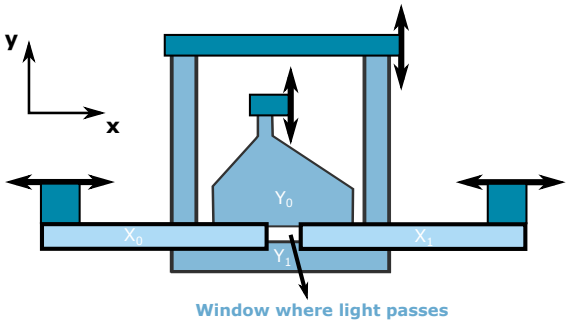

Fig. 4. Typical reticle masking blades of a lithography machine.

A. Photolithography Machines

Photolithography is the principal manufacturing process in the semiconductor industry, where a pattern printed on a transparent substrate, knows as the reticle, is exposed onto a silicon wafer. The high precision is required for the ability to project a fine image of extremely small features onto the wafer. The current resolution is within the nanometer scale [11]. The semiconductor industry's continuous need for higher resolution, i.e, smaller and faster chips, and higher throughput, i.e., cheaper process, led to huge advances in the lithography process. In the lithography machine the reticle and wafer perform fast motions with high precision relative to each other, while the exposure of the wafer is performed through a slit of light passing through the reticle. The commonly used light source is deep ultraviolet light, while recently extreme ultraviolet light (EUV) has been introduced which allows the fabrication of pattern features up to few nanometers. Many variables define the performance of the lithography process such as the resolution, overlay, and focus, which all directly impact the final integrated circuit's size, speed, and performance. To maximize throughput, these machines operate at very high accelerations, which provide high scanning speeds while maintaining the required accuracy. An illustration of an EUV based lithography machine is shown in Fig. 3.

B. Reticle Masking Unit

The Reticle Masking (Rema) is the unit within a lithography machine which is responsible for masking light except for an arbitrary sized window in an arbitrary position. This is usually accomplished through four independent blades, two moving in X direction and two in Y direction. The function of masking light comes into play during the exposure of the reticle onto the wafer, where light should be projected only on a desired part of the reticle. This allows the reticle to contain more then one image of layers of products. To expose a single image, hide the rest of the reticle using the reticle masking blades. Similar to the reticle, these blades perform high precision accelerations. Fig. 4 shows a top view illustration of the reticle masking where light passes only through the window between the blades.

C. Problem Formulation

During typical operation of the reticle masking unit, linear X and Y blade motions cause undesired Z vibrations of the blades

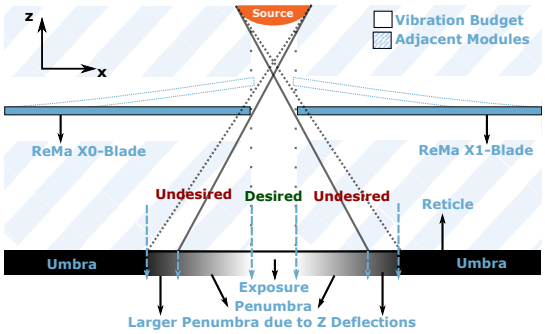

Fig. 5. Z vibrations of the X-blade lead to larger penumbra on the exposed wafer.

due to the non-ideal actuation. These Z deflections cause larger penumbra, which is partial masking of the light instead of complete masking. Penumbra leads to defocus where the exposure overlaps a portion of the neighboring field to the current exposed field. This is one of the limiting factors of high volume manufacturing which requires that no empty space remains unused. This phenomena which is increased by vibrations is demonstrated in Fig. 5. Additionally, vibrations lead to tighter manufacturing tolerances due to the limited budget with the modules above and below the blades. For simplicity, X-blades with a simplified geometry are considered in this work.

Vibration damping is considered as an appropriate solution that can deal with the typically lightly damped system. Moreover, the recent EUV based lithography machines lack air damping (vacuum operation) leading to even sharper resonance peaks. Piezoelectric transducers compactly embedded on the blade offer a suitable approach for vibration damping. Piezoelectric passive shunt damping synthesized using powered virtual inductors is one solution. Active feedback damping is another powered approach which is expected to improve performance and robustness. From a feasibility aspect, the high accelerating blade imposes restrictions on connecting physical wiring with the fixed world for power supply. This motivates the need of a self-powered piezoelectric vibration damping solution.

This work aims to achieve vibration damping of the reticle masking X-blade during scanning motions using embedded piezoelectric materials which either realize a passive or an active damping behaviour in a self-powered approach.

III. System Identification & Modeling

An experimental reticle masking test-rig has been adapted for the following application. A reticle masking blade is clamped to a mover performing scanning motion as shown in Fig. 6. In this section, the flexible reticle masking blade during scanning motion is modeled. Firstly, structural vibration analysis is performed on the blade independently. Afterwards, a model of the blade with embedded piezoelectric transducers is derived and validated. The coupling between the scanning motion and the Z-vibrations is then identified. Finally, the dominant vibrations are analyzed for typical excitation.

A. Blade Structural Vibration Analysis

The reticle masking blade can be dynamically modelled as a cantilevered flexible structure resulting in a model represented in modal coordinates. An Euler-Bernoulli beam model is firstly derived (Appendix I-B). This was chosen over a Timoshenko model due to the thin beam assumption based on the small slenderness ratio of the blade (Appendix I-C). Afterwards, a Finite Element Method (FEM) based analysis is performed, to validate the accuracy of the beam assumption relative to $2D$ (plate) or $3D$ models.

A stainless steel AISI 304 blade is used, the dimensions and material properties are shown in Table I. The Euler-Bernoulli exact solution for the cantilevered beam is derived for the mode shapes $\phi_i(x)$, over the length x, and modal frequencies ω_i in Equations 1 and 2, respectively, where i denotes the number of mode.

$$\begin{aligned}\phi_i(x) =& A_i[\sin(\beta_i x) - \sinh(\beta_i x) - \frac{\sin(\beta_i L) + \sinh(\beta_i L)}{\cos(\beta_i L)} \\ & * (\cos(\beta_i x) - \cosh(\beta_i x))]\end{aligned} \tag{1}$$

Where L is the length, A_i a scaling factor, and β_i solved numerically for $i = 1, 2, 3$ as $\beta_i = [1.875, 4.694, 7.855]$.

$$\omega_i = \sqrt{\frac{EI}{L^4 m}}(\beta_i L)^2 \tag{2}$$

Where E is the Young's modulus, I the moment of inertia derived using the width W and thickness H. The mass per unit length m is calculated using the density ρ. Additionally, the shear modulus G is used in FEM. The results of FEM are shown in Fig. 7 for the frequency range of interest $(0 - 1k\,Hz)$. The first three bending modes clearly match the Euler-Bernoulli beam's mode shape assumption, with some uncertainty in the modal frequency. The uncertainty increases for higher modes, however, is around $4\,Hz$ for the first mode. Moreover, the Euler-Bernoulli misses the torsional mode as expected, which is predicted by the FEM to be at $538.6\,Hz$ with modal amplitude of $5 \times 10^{-5}\,m$. Therefore, the Euler-Bernoulli beam assumption is valid to a large extent with negligible error due to the torsional mode which has modal amplitude 3 orders of magnitude smaller, relative to the first three bending modes. This is due to the large aspect ratio (Appendix I-D).

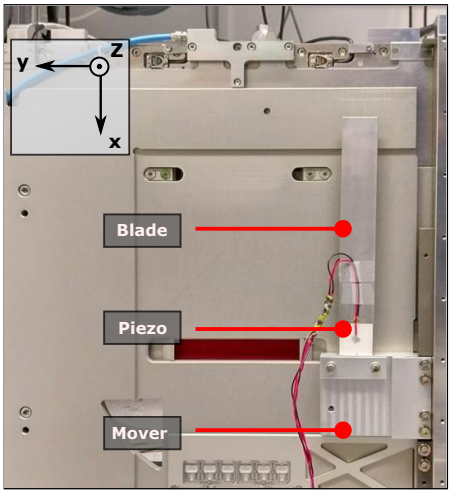

Fig. 6. Photo of the piezo embedded blade clamped to the linear actuator within the reticle masking test-rig.

TABLE I
Beam Dimensions and Properties

Parameter	Value	Unit	Parameter	Value	Unit
L	219	$[mm]$	E	197	$[GPa]$
W	32	$[mm]$	G	86	$[GPa]$
H	2.5	$[mm]$	ρ	8	$[g/cm^3]$

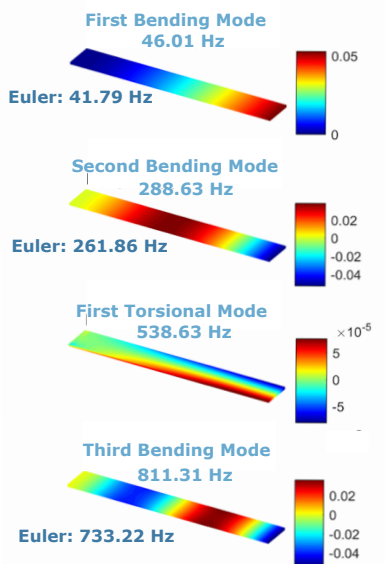

Fig. 7. Vibration analysis of the flexible cantilevered structure.

The collocated transfer function from a force actuator to a displacement sensor, located at x_a, of the first three bending modes could be represented by $G_s(s)$:

$$G_s(s) = \frac{Z(s)}{F(s)} = \sum_{i=1}^{3} \frac{\phi_i^2(x_a)}{s^2 + \omega_i^2} + R \tag{3}$$

Where R approximates the contribution of the residual modes which are truncated, and $\phi_i(x_a)$ is the modal amplitude at the actuation location. The mode shapes are normalized with respect to the modal masses μ_i.

B. Embedded Piezoelectric Transducers

In this section, piezoelectric transducers which are embedded on the reticle masking blade are firstly introduced. Optimal choices for placement and sizing are then discussed. Finally, the piezo-blade embedded structure is modeled and the relevant transfers are derived.

1) Piezoelectric Transducers: Piezoelectric materials have the ability to convert mechanical energy into electrical energy and vice versa, i.e, electromechanical transduction. The piezoelectric effect could be "direct" where the transducer generates an electric charge proportional to a mechanical stress to which it is subjected. The inverse piezoelectric effect occurs when an electric field is applied into the material causing a proportional strain to that field.

Piezoelectric elements behave in three modes, d_{31}, d_{33}, and d_{15}. In d_{31} mode (transverse) the electric field is applied parallel to the polarization while the deformation is perpendicular to the polarization direction. Simultaneously, in d_{33} mode (longitudinal) by applying the same parallel electric field, a deformation parallel to the polarization direction occurs. In contrast, the d_{51} mode (shear) produces shear deformation when subjected to an electric field perpendicular to the polarization direction [12].

The constitutive equations of the piezoelectric transducers are derived in order to model its electromechanical behavior. Restricting the analysis to one direction allows expressing the equations using scalars rather than tensors [12]:

$$\begin{bmatrix} S \\ D \end{bmatrix} = \begin{bmatrix} s^E & d \\ d & \epsilon^T \end{bmatrix} \begin{bmatrix} T \\ E \end{bmatrix} \tag{4}$$

Where S is the strain, D the electric displacement, T the applied stress, and E the electric field. The material constants ϵ^T, s^E, and d represent the permittivity under constant stress, compliance for constant electric field, and piezoelectric charge constant, respectively. Additionally, different forms of the constitutive relations exist by using different quantities as independent variables. Switching the independent variables introduces the coupling coefficient k which represents the electromechanical conversion ratio:

$$k^2 = \frac{d^2}{s^E \epsilon^T} \tag{5}$$

Electrical quantities are defined under constant stress T or deformation S. Similarly, mechanical quantities are defined under constant electrical displacement D, or field E. These are denoted by a superscript. The subscript defines the utilized mode, e.g., d_{31}, k_{31}. Additionally, the generalized electromechanical coupling coefficient K_i represents the electromechanical coupling factor of the piezo embedded in a structure to a certain vibration mode i. This constant is derived experimentally in practice using:

$$K_i^2 = \frac{\Omega_i^2 - \omega_i^2}{\omega_i^2} \tag{6}$$

Where Ω_i and ω_i represent the structure's modal frequency with the piezo having open and short circuit conditions, respectively.

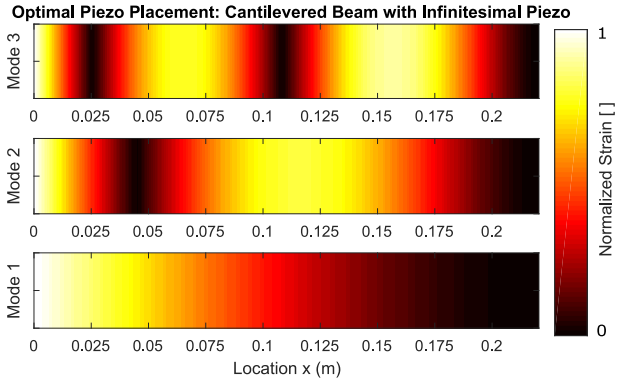

Fig. 8. Optimal placement of an infinitesimal piezo patch onto the cantilevered beam clamped at $x = 0$. According to the color map, black and white correspond to the lowest and highest performing locations, respectively.

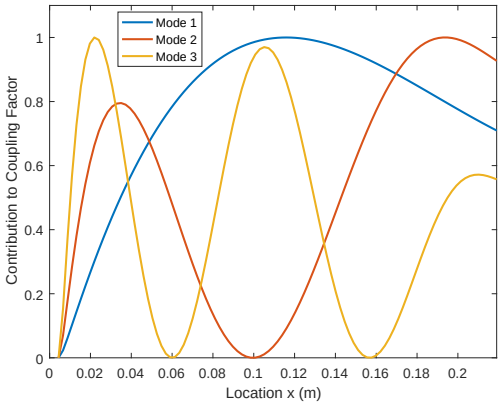

Fig. 9. Length contribution to the electromechanical coupling factor based on an analytical finite length piezo analysis. The first end of the piezo is at $x = 0$.'

The capacitance under constant force C^F of a piezoelectric element with length l_p, width b_p, and thickness t, can be derived using:

$$C^F = \frac{\epsilon_{33}^T b_p l_p}{t} \tag{7}$$

Accordingly, the blocked capacitance under constant deformation/strains is:

$$C^x = C^F(1 - k_t^2) \tag{8}$$

Where k_t is used instead of k_{33} in the absence of lateral strains only, i.e., free expansion in other directions.

In this application, the piezoelectric elements are mounted on the blade utilizing the d_{31} mode; the subscript 31 which defines the mode of operation is dropped for simplicity.

2) Optimal Placement & Sizing: The location of the embedded piezoelectric elements has a great influence on the generalized electromechanical coupling between the transducers and the vibration modes of interest. This relation is analyzed in order to reach the optimal placement which enhances the coupling and accordingly maximize application performance.

Firstly, it is worth noting that this analysis depends primarily on the type of transducer considered. For example, the optimal placement of an accelerometer (sensor) or a tuned mass damper would typically exist at the maximum displacement

amplitude of vibration, i.e., the beam tip. However, this is not the case for piezoelectric transducers mounted onto the beam, utilizing d_{31} mode.

The embedded piezo in d_{31} mode applies a bending moment M on the beam, therefore, it could be deduced that for an infinitesimal piezo the coupling factor is directly proportional to the second derivative of the bending displacement, i.e., curvature, using the following relation from the mechanics of materials:

$$M(x,t) = EI\frac{\partial^2 z(x,t)}{\partial x^2} \tag{9}$$

For a piezo with finite length, this is proportional to the relative rotation between its ends, which is also the difference of the first derivative of the bending displacement . The first and second derivatives of the first three mode shapes are shown in Appendix I-E.

Considering the infinitesimal analysis, the absolute value of the second derivative of the mode shape is shown in Fig. 8, to determine the optimal placement relative to the targeted mode(s). To this end, it could be concluded that placing the piezoelectric transducers at the clamped end achieves the highest performance, relative to the first three bending modes. Lowest coupling exists at the tip and the nodes of the modes.

The piezoelectric transducer optimal sizing is analyzed to determine the dimensions of the piezo element. The width is desired to be along the full width of the beam, in order to maximize the coupling factor, as well as to avoid any excitation of the torsional mode. The length contributes analytically to the coupling factor through an inversely proportional term, and a directly proportional length dependent term (Appendix I-E1). The latter is the relative rotation of the mode shape evaluated at the ends of the piezo element. Accordingly, the net contribution of the piezo length to the coupling factor with one end attached at the clamp is shown in Fig. 9.

It could be deduced that the performance targeting the first mode could be improved by increasing the length up to around 50% of the blade length, which matches the numerical analysis of [13].

3) Embedded Piezo Blade: The dimensions and material properties of the piezo element embedded on the blade are given in Table II. The length l_p was determined based on the previous analysis, but also on commercial availability.

Firstly, a rectangular embedded piezo element is considered as an actuator as shown in Fig. 10. Assuming the voltage difference on the piezo electrodes is controlled, the applied moment on the blade at the piezo ends is derived using Hamilton's principle as [1]

$$M_p = -e_{31} b_p z_m V = g_a V \tag{10}$$

Where z_m is the distance from blade's mid-plane, and $e = d/s^E$.

Similarly, the piezo element is treated as a sensor, where strain causes electric displacement according to the constitutive equations. Connecting the piezo to a charge/current amplifier enforces short circuit conditions. Thus the sensor forms a dual relation with the piezo actuator as:

$$Q = -e_{31} b_p z_m \Delta\theta_i = g_s \Delta\theta_i \tag{11}$$

TABLE II
PIEZO DIMENSIONS AND PROPERTIES

Parameter	Value	Unit	Parameter	Value	Unit
l_p	29.97	$[mm]$	$-d_{31}, d_{33}$	$208, 443$	$[pC/N]$
b_p	29.97	$[mm]$	$k_{31}, k_{33},$	$0.38, 0.74$	$[\,]$
t	0.508	$[mm]$	k_t	0.5	$[\,]$
C^F	26.9	$[nF]$	s^E_{11}, s^E_{33}	$16, 19$	$[\mu m^2/N]$
C^x	19.6	$[nF]$	$\epsilon^T_{33}/\epsilon_0$	1900	$[\,]$

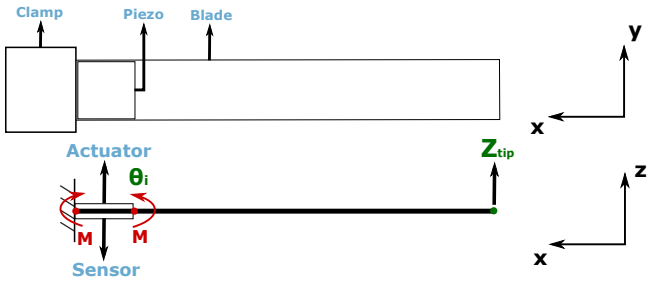

Fig. 10. Schematic of the blade with collocated embedded piezoelectric actuator and sensor.

Where $\Delta\theta_i$ is the relative rotation at the piezo ends, and Q the piezo charge. Therefore, Q is directly proportional to the relative rotation, where $\Delta\theta_i = [10.52, 49.28, 97.36]$. Consequently, the charge amplifier generates a voltage V_s which is proportional to Q:

$$V_s = -\frac{Q}{C_o} \tag{12}$$

Where C_o is the charge amplifier capacitance.

Accordingly, a collocated actuator/sensor transfer function could be established from Equations 10 and 11. An actuator/sensor pair extending over the same length of the beam are shown in Fig. 10. Therefore, the transfer function between the voltage applied on the actuator piezo, and the output voltage of the sensor piezo is:

$$G_{vv}(s) = \frac{V_s}{V_a} = g_a g_s \sum_{i=1}^{3} \frac{\Delta\theta_i^2}{s^2 + \omega_i^2} \tag{13}$$

Moreover, for the identical actuator and sensor $g_a = g_s = -0.0021$.

Additionally, the transfer function between the Z tip deflections and voltage applied by an actuator piezo could be defined as:

$$G_{yv}(s) = \frac{Z}{V_a} = g_a \sum_{i=1}^{3} \frac{\Delta\theta_i \phi_i(x_t)}{s^2 + \omega_i^2} \tag{14}$$

Where $x_t = 0.219$. Both transfers are represented in the block diagram in Fig. 11. Noting that $G_{yv} = G_{vf}$, where G_{vf} is the transfer between a sensor piezo and a force actuator.

The root locus and open loop Frequency Response Function (FRF) for the transfer G_{vv} could be then shown in Fig.'s 12 and 13, respectively. An interesting property observed is the alternating pole zero pattern in the root locus, or the resonance anti-resonance in FRF. This property which is due to collocation has great influence on robust controller design.

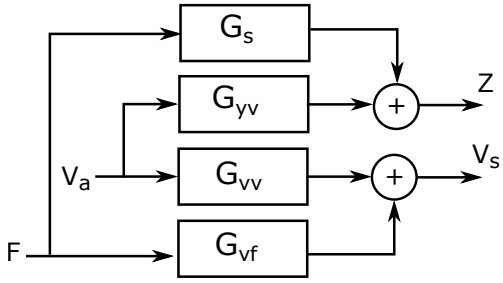

Fig. 11. Block diagram of the different transfer functions within the piezo embedded blade structure.

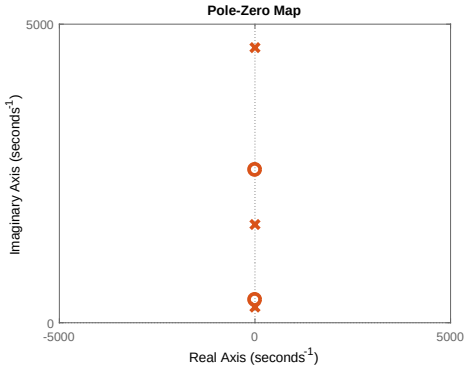

Fig. 12. Pole zero map of the G_{vv} transfer showing the alternating pole zero pattern. The upper symmetric half is only shown.

C. Blade identification

The blade dynamics are identified using the piezoelectric actuator/sensor pair in order to validate the modal analysis and model derived in Sections III-A and III-B, respectively.

The first transfer to be identified is the $G_{vv} = V_s/V_a$ transfer which clearly identifies the vibration modes of the blade. The first piezo V_a is excited by a periodic $10\,V$ sine sweep with a bandwidth of $1 - 1.25k\,Hz$. The voltage output of the second collocated piezo V_s is measured. Accordingly, the FRF is estimated and the magnitude shown in Fig. 13.

The modelled first three bending modes are clearly identified. Additionally, the inherent (material) damping could be estimated as $\zeta_{in} = [0.01, 0.03]$. Inherent damping is appended to the Euler-Bernoulli model. Another important aspect is the unmodelled feedthrough arising from modal truncation and actuator/sensor crosstalk, this term alters the frequency of the zeros [1], [14]. This is compensated by estimating $R = 0.01$. Due to unmodelled non-linearities, an additional gain mismatch is compensated in this model.

The second identification is the G_{yv} transfer. One piezo V_a is excited by the previous sine sweep, and the absolute Z displacement of the blade tip is measured using an optical sensor. The FRF is estimated in Fig. 14.

The identified G_{yv} transfer which matches the model, validates that the absolute displacements are vibrations caused by the blade flexibility. This FRF is used afterwards as a performance measure of the damping introduced by the proposed solutions. This measurement has more noise as the optical sensor measures Z, the absolute displacement of the

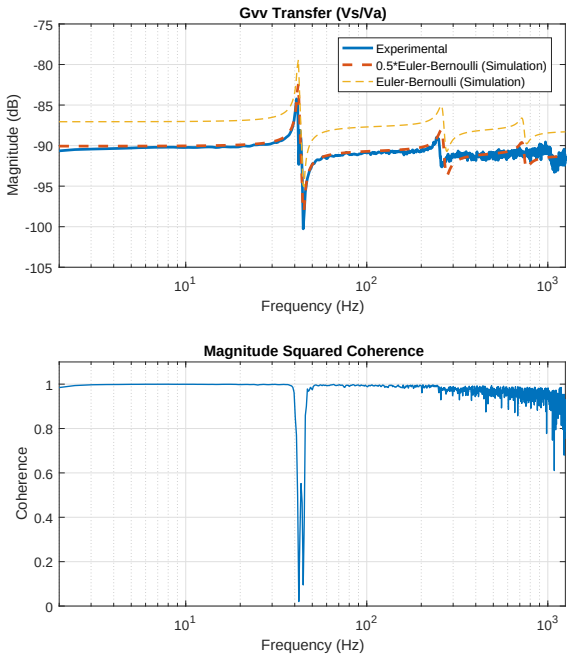

Fig. 13. Estimated G_{vv} transfer (Experimental) versus Euler-Bernoulli beam model (Simulation) shows the blade's first three bending modes.

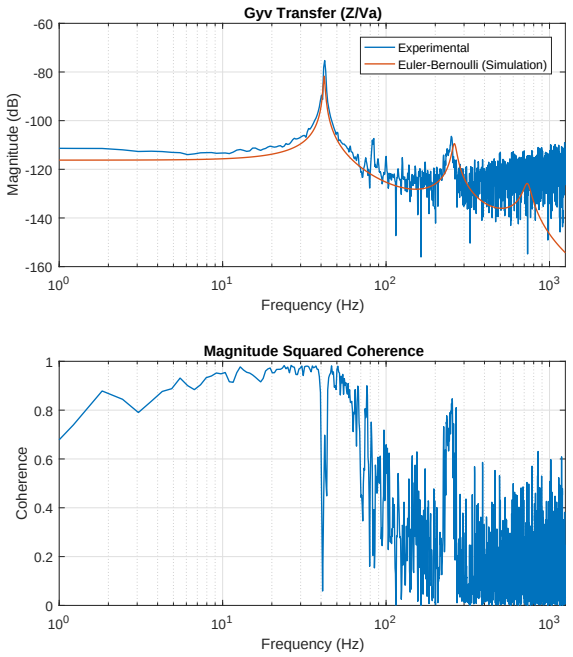

Fig. 14. Estimated G_{yv} transfer (Experimental) versus Euler-Bernoulli beam model (Simulation) shows the dynamics between the Z displacement and piezo actuator V_a.

blade tip, rather than V_s which only captures the relative deformation between the blade tip and clamp.

The generalized coupling factor is evaluated experimentally using the open and short circuit conditions as $K_1 = 0.03$.

D. X-Z Coupling Identification

So far, the blade has been modeled as a flexible cantilevered structure. The next step is to include the scanning X motion to the Z deflections coupling. Scanning in the X produces Z displacement of the blade tip measured by the optical sensor. This coupling arises due to the non-ideal actuation where the actuating force does not exactly pass through the center of mass. This is considered as a base excitation which causes base displacement, tilting, or both. The base acceleration $\ddot{Z}_b(t)$ excites the vibration modes of the blade. The schematic in Fig. 15 shows the model including the $X - Z$ coupling. Fig. 16 shows the block diagram of the model.

In order to verify this model, the FRF is estimated between the servo actuator input force applied on the mover F_x, and the outputs: mover X displacement and blade tip Z displacement. Additionally, the latter FRF is compared to the FRF between an actuator piezo V_a and blade tip Z displacement. The results are shown in Fig. 17.

It could be concluded that the input force F_x produces Z displacement similar to that due to applying voltage V_a on the piezo actuator. The applied voltage V_a produces a moment near the clamped end, i.e., the spatial derivative of bending displacement in Z at the tip. Therefore, X motion produces base excitation of the blade in the Z direction. Moreover, no additional resonances were observed in Z/F_x, hence the mover could be regarded as rigid body. The FRF between F_x and X shows typical moving mass behavior, which is servo controlled, and is shown for clarity.

E. Blade Vibrations for Typical Excitation

As a typical application for reticle masking, two motion profiles are introduced in this section, and are denoted as typical excitation. The first is a single step motion and the second is scanning motion. The frequency content of the acceleration profiles, which excite the vibration modes is shown in Fig. 18. The position, velocity, and acceleration setpoints of the step and scanning motion profiles are shown in Fig.'s 19 and 21, respectively.

The blade is excited using both profiles where for the scanning motion 100 scans are performed. The settling response of the blade tip vibrations is measured using the optical sensor starting at the end of each profile. Syncing of different measurements is shown in Appendix IV-B. The response for the step and scanning motions is shown in Fig.'s 20 and 22, respectively.

In the time domain, the background noise before excitation has a peak amplitude of $2\mu m$. A typical excitation causes peak amplitudes of $7\,\mu m$ and $48\,\mu m$ for step and scanning motions, respectively. In the frequency domain the Power Spectral Density (PSD) and Cumulative PSD (CPSD) have been calculated. From the spectral analysis, it can be concluded that the first bending mode is the dominant cause of blade vibrations for typical excitation. The background noise has a flat spectrum and is uncorrelated (Appendix IV-A), which makes it white noise. Scanning motion additionally excites the second bending mode however this has no significant contribution to the CPSD.

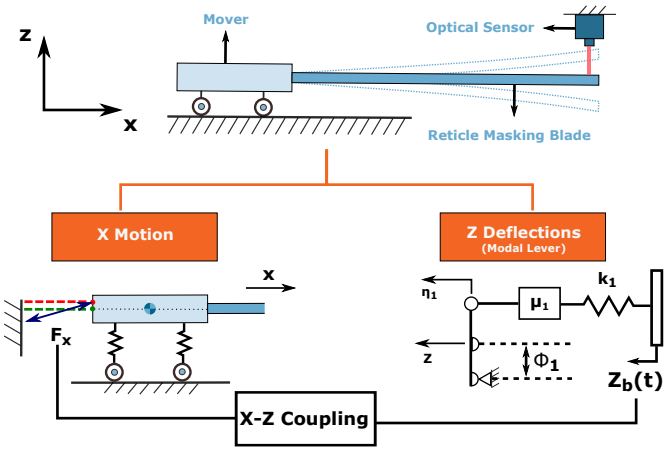

Fig. 15. Model representing the coupling between the X motion and the Z deflections considering the first bending mode.

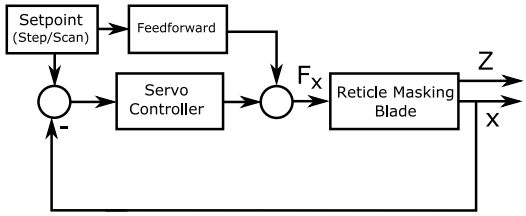

Fig. 16. Block diagram of the transfer between the input force and outputs.

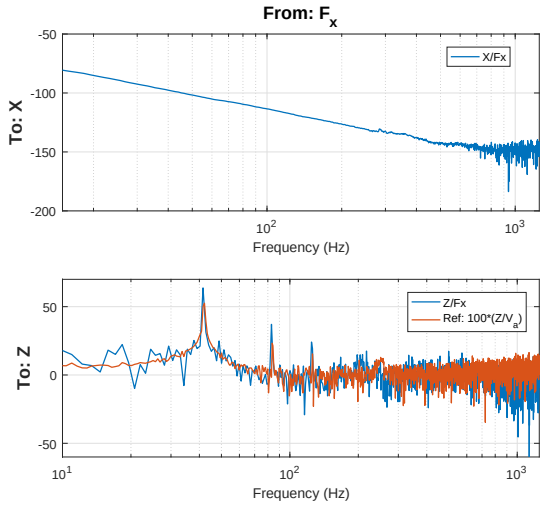

Fig. 17. FRF between input forces and output displacements shows the $X-Z$ coupling.

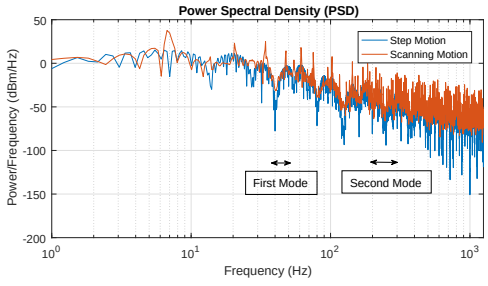

Fig. 18. Frequency content of the acceleration profile for typical excitation.

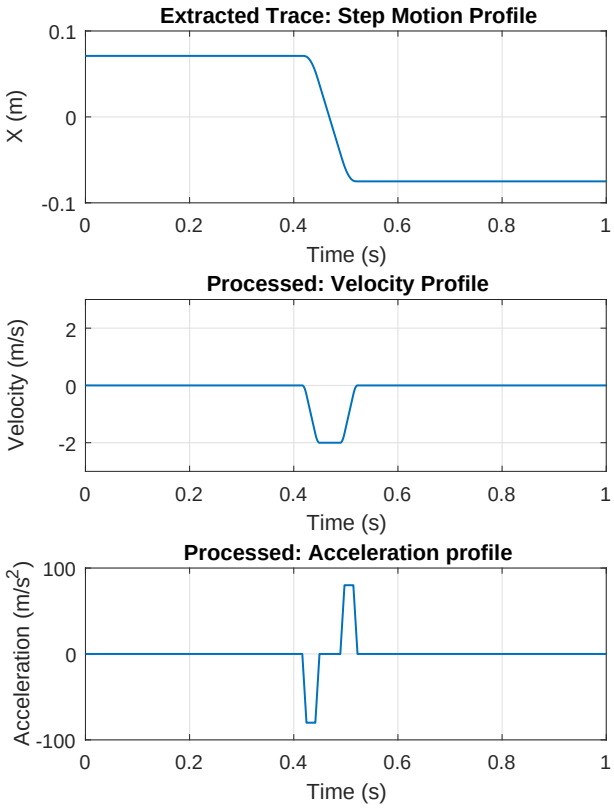

Fig. 19. Step motion profile as a typical excitation of the reticle masking blade.

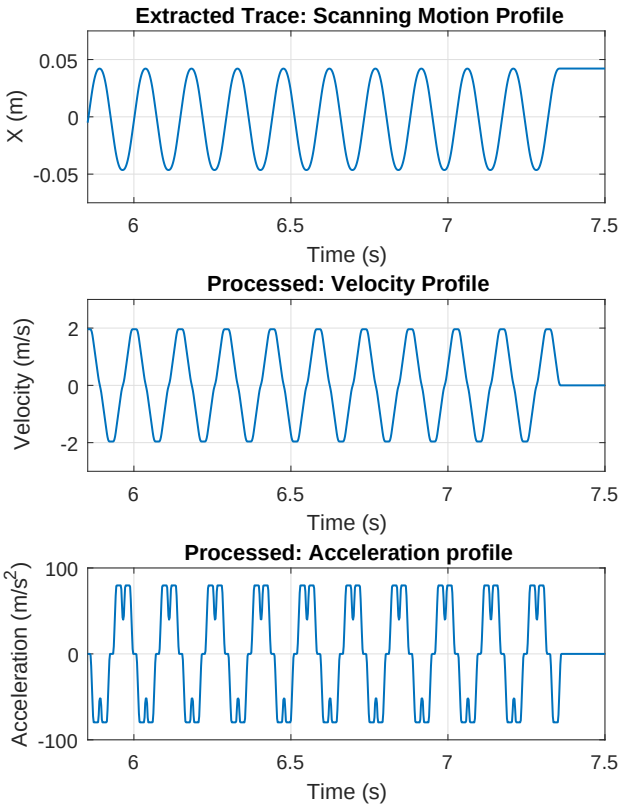

Fig. 21. Scanning profile of 100 scans as a typical excitation of the blade. Last 10 scans are shown, previous scans were omitted for clarity.

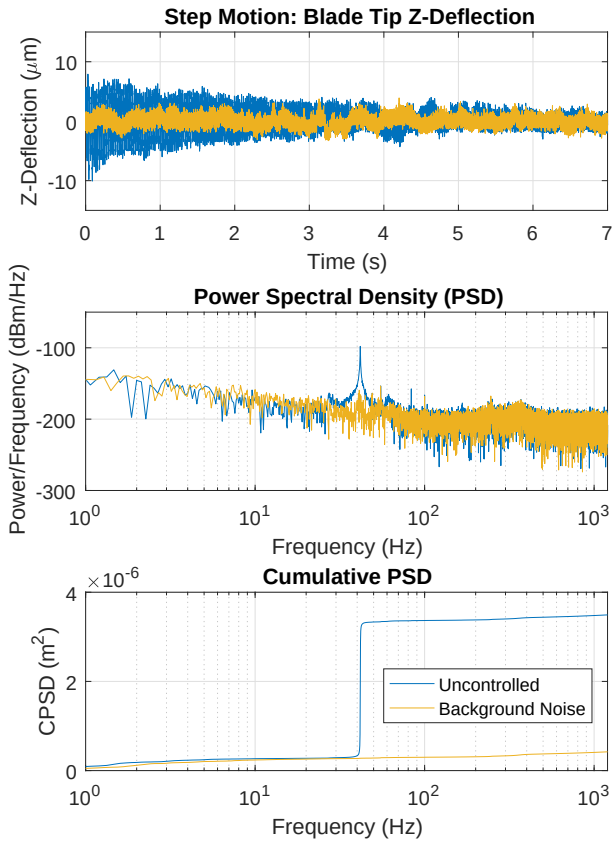

Fig. 20. Spectral analysis of the blade tip Z vibrations after step motion excitation.

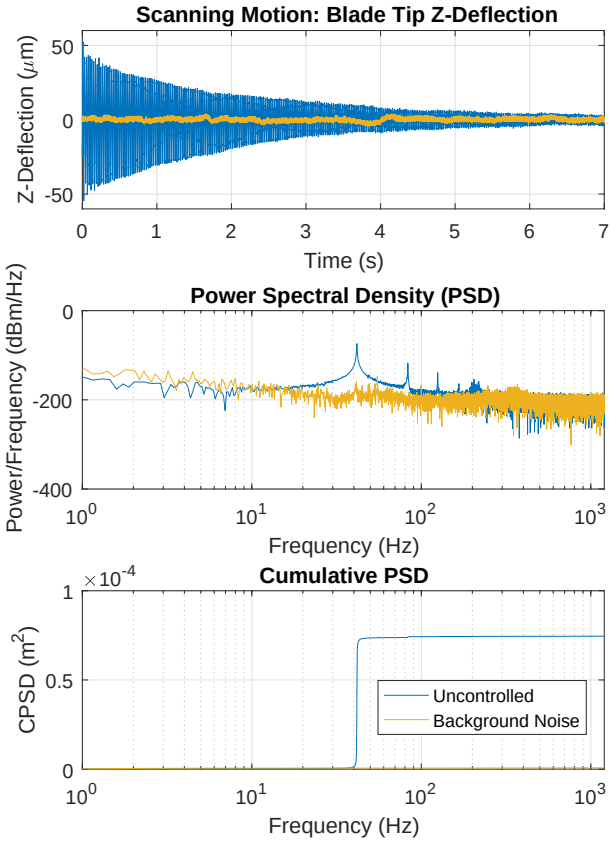

Fig. 22. Spectral analysis of the blade tip Z vibrations after scanning motion excitation. (Note: scales differ between this figure and Fig. 20.)

IV. Passive Shunt Damping

In this section, damping structural vibrations using piezoelectric materials shunted with passive electrical circuits is discussed. Afterwards, realizing a virtual inductance through gyrators implemented using active components is presented.

A. Tuning of the Passive Shunt

Piezoelectric passive shunts achieve damping by connecting an electrical impedance with high damping characteristics to the piezoelectric. The piezoelectric coupled to the mechanical structure performs electromechanical transduction to dissipate the vibrational energy through the electrical circuit. The simplest form of shunting is the resistive shunt, which however can only provide very little damping to the system [1], [4]. Resonant (RL) shunting consists of a resistor R and an inductor L to form an RLC circuit along with the capacitance of the piezoelectric [1], [4], [15], [16]. The inductor is tuned such that the electrical resonance matches the mechanical resonance. Accordingly, R is adjusted to provide the maximum achievable damping to the mechanical structure.

This analysis is limited to single mode RL shunting since only one mode is dominant in the system. The operation of an RL shunted piezoelectric is analogous to a tuned mass damper [3], more specifically a skyhook tuned mass damper [17]. In both techniques, a second order system appends the structure to enhance the damping properties for a specific frequency band.

The resonance frequency of the electrical circuit is defined by:

$$\omega_e^2 = \frac{1}{LC^F(1-k_t^2)} \tag{15}$$

Since the electrical resonance ω_e should match the targeted mechanical mode ω_i, therefore, the inductor L is tuned such that:

$$L = \frac{1}{\omega_i^2 C^F(1-k_t^2)} \tag{16}$$

The blocked capacitance $C^F(1-k_t^2)$ will be denoted by C_p for simplicity. Similarly, an optimal tuning law for the resistance value has been derived using root locus technique [1]:

$$R_L = 2L\omega_i K_i \tag{17}$$

In order to asses the performance of passive resonant shunting, the theoretical maximum achievable damping of an optimally tuned RL shunt is derived in [1]:

$$\zeta_{RL} = \frac{K_i}{2} \tag{18}$$

For the sake of completion, the theoretical maximum achievable damping for an optimally tuned resistive shunt is:

$$\zeta_R = \frac{K_i}{2}\zeta_{RL} \tag{19}$$

Which is indeed low compared to the damping achieved with an RL shunt, considering that K_i

Accordingly, the tuned passive RL shunt is evaluated to target the first bending mode of the blade such that:

$$\begin{aligned} L &= 728.35\ H \\ R_L &= 12.08\ k\Omega \end{aligned} \tag{20}$$

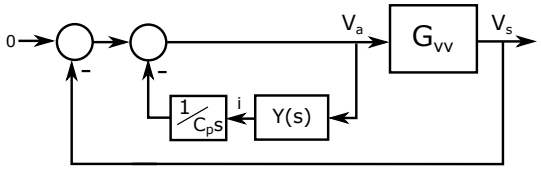

Fig. 23. Interpretation of passive shunting as a feedback structure of the transfer $G_{vv}(s)$.

From another perspective, passive shunting could be interpreted as a feedback system structure [4]. This facilitates the comparison of the simulation of a passive shunting versus different damping approaches in response to excitations. The feedback interpretation of passive shunting is shown in Fig. 23. This could be proved by shunting the sensor piezo with an admittance $Y(s)$. The voltage over the shunt V_z is:

$$V_z(s) = V_s(s) - \frac{1}{C_p s} I_z(s) \tag{21}$$

Where I_z is the current flowing through the shunt. Substituting $I_z = V_z Y(s)$ yields:

$$\frac{V_z(s)}{V_s(s)} = \frac{C_p s}{C_p s + Y(s)} \tag{22}$$

In the case of the sensor piezo having open circuit ($Y(s) = 0$):

$$V_z(s) = V_s(s) = G_{vv}(s) V_a(s) \tag{23}$$

However, if the shunt has finite impedance, the linear superposition hold as:

$$V_s(s) = G_{vv}(V_a(s) - V_z(s)) \tag{24}$$

By substituting equation 22 into equation 24:

$$V_s(s) = G_{vv}\left(V_a(s) - \frac{C_p s}{C_p s + Y(s)} V_s(s)\right) \tag{25}$$

Finally, the transfer between the shunted sensor piezo and the actuator piezo reads:

$$\frac{V_s(s)}{V_a(s)} = \frac{G_{vv}(s)}{1 + G_{vv}(s)K(s)} \tag{26}$$

Where $K(s)$ is the interpreted feedback controller:

$$K(s) = \frac{C_p s}{C_p s + Y(s)} \tag{27}$$

Based on this feedback model of the passive shunt, the Bode plot for various tuning values is shown in Fig.24. The achieved damping with optimal tuning versus over/under damped tuning and open/short circuit conditions is clearly shown. It could be concluded that $14\ dB$ of first mode resonance attenuation is achieved, which is equivalent to damping of $\zeta_{RL} = 0.012$, in Fig. 25 for the G_{yv} transfer.

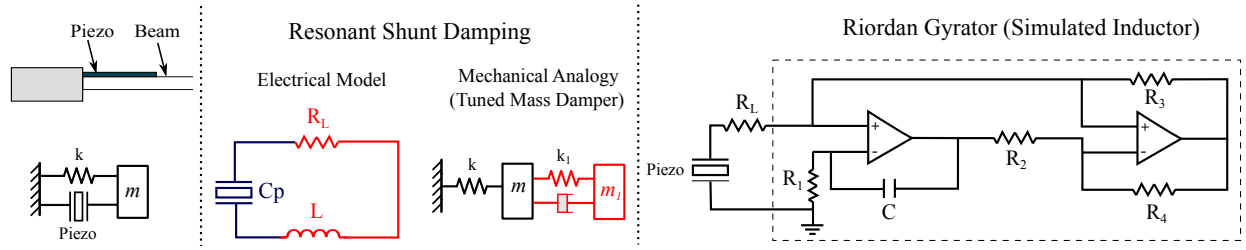

Fig. 26. Resonant (RL) shunting achieves damping similar to mechanical tuned mass dampers but through a compact configuration. Large inductance values can be feasibly implemented using gyrators, e.g., Riordan Gyrator, however the utilized op-amps require power for operation.

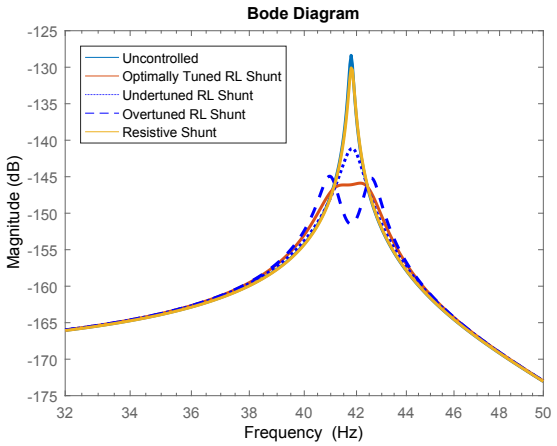

Fig. 24. Optimal tuning of the RL shunt achieves first mode damping for the G_{vv} transfer versus detuned and open/short circuit conditions (uncontrolled).

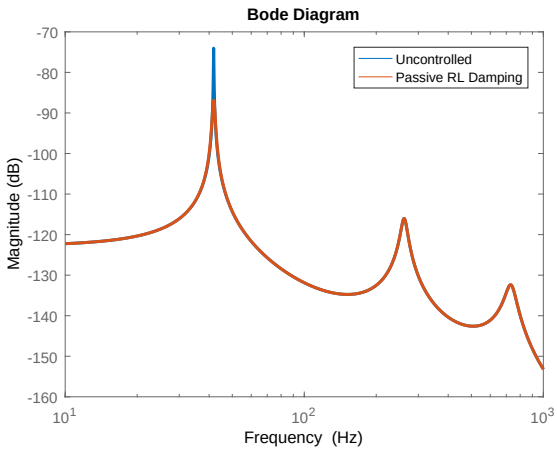

Fig. 25. Magnitude Bode plot of the damped G_{yv} transfer with RL passive shunt targeting the first mode.

B. Virtual Inductance

High inductance values required for resonant shunts is not realizable using coils or physical inductors. This could be identified from Equation 16 where the optimal inductance value is inversely proportional to the resonance frequency and piezo capacitance. The first is low frequent, in order of magnitude of $10^2\ rad/s$, while the latter is of 10^{-9} to $10^{-6}\ F$. Therefore, typical inductance values are in terms of hundreds/thousands of henries.

Passivity is a characteristic inherent to passive damping, as ideally no energy is supplied to the system, thus stability is guaranteed. This characteristic is not violated by the fact that energy is required for powering op-amp circuits which synthesize the inductance. Although active components are involved, still this is referred as "Passive" in the literature.

A gyrator circuit proposed by Riordan could be utilized to simulate high quality inductors [5], as shown in Fig. 26. The Riordan gyrator is based on differential amplifiers, and flips the effort and flow of the input with a tunable gyration ratio, $g = R$, in the case of $R_1 = R_2 = R_3 = R_4 = R$. Accordingly, a capacitive input impedance of $Z_{in} = C$ becomes inductive with an inductance L of:

$$L = CR^2 \tag{28}$$

The gyrator resistor is chosen to be $R = 10\,k\Omega$. The capacitor of the gyrator is tuned in order to simulate the inductance in Equation 20:

$$C = \frac{L}{R^2} = 7.28\,\mu F \tag{29}$$

It is worth noting that this approach simulates non-floating (grounded) inductors.

This passive shunting approach could be extended to multi-modal damping using a shunt circuit consisting of multiple resistors and inductors such as the Holkampp circuit [4]. However, synthesizing these multiple inductors is done using gyrator circuits which form floating inductors [4].

C. Simulations

A Simulink model is developed in order to simulate the damped versus undamped response against the typical excitation of step and scanning motions. The Z displacement time response is shown starting from the beginning of the step/scanning motions then the settling time after the excitation stop.

In the time domain, the vibration peak amplitude during the scanning motion is reduced from $50\ \mu m$ to $15\ \mu m$. This is clearly achieved from the dominant mode attenuation of $66 dBm/Hz$ in the spectral analysis. Similarly, for step motion $39\ dBm/Hz$ attenuation is achieved.

Simulations using the gyrator (ideal op-amps) instead of an ideal L yield the same results, verifying the functionality of the simulated inductor.

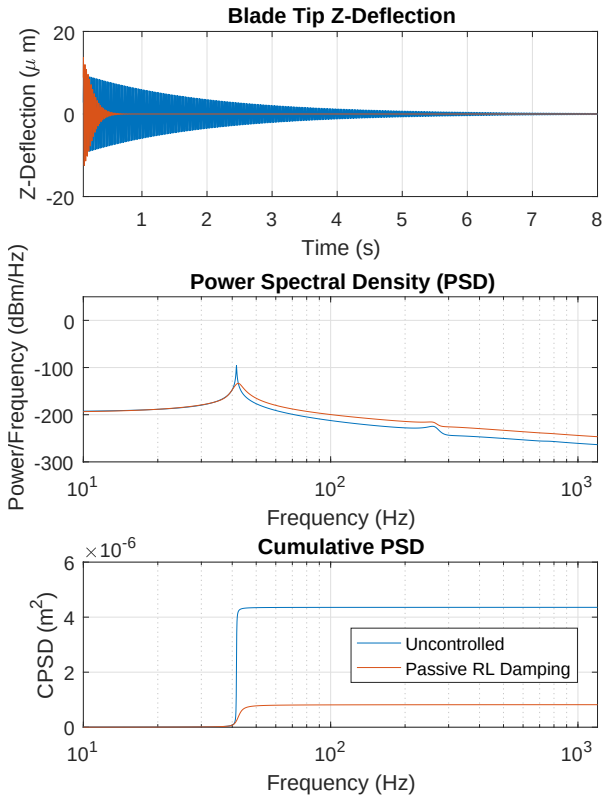

Fig. 27. Simulated spectral analysis of the passive damped blade tip Z vibrations for step motion excitation.

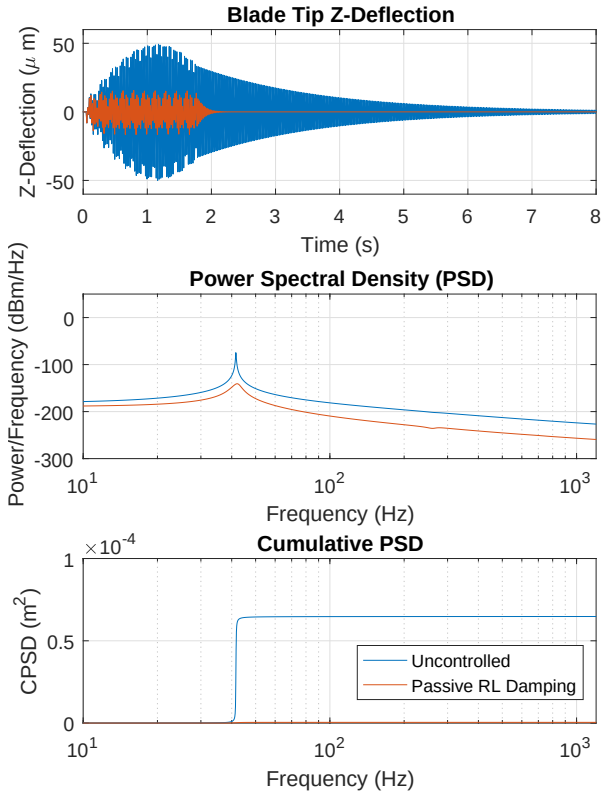

Fig. 28. Simulated spectral analysis of the passive damped blade tip Z vibrations for scanning motion excitation.

V. Active Damping

In this section, active feedback controllers which primarily enhance the damping properties of the system are discussed. This is equivalent to shifting the real part of the poles to the negative half plane, or attenuating the resonance peaks in the frequency domain, while maintaining the natural frequencies unaltered.

Collocated sensors and actuators are considered for active feedback as they always lead to alternating poles and zeros. This property allows the realization of controllers robust against uncertain system parameters, or moreover, passivity-based controllers which typically achieve unconditional stability [1], [18]. Additionally, collocated control is advantageous for its simplicity where the control laws require little or no knowledge of the system (knowledge of the natural frequencies at most), i.e., measuring the open loop frequency response is followed by tuning intuitive controller parameters [1], [19]. Non-collocated control on the other hand requires model-based feedback controllers which have its stability dependent on damping. For the typically lightly damped system, small variations in the system parameters can easily destabilize these controllers [1].

Considering the system transfer, a force actuator can be collocated with a translation sensor measuring velocity or displacement. The first is achieved through a current amplifier attached to the piezoelectric element, while the latter through a charge amplifier. Using a velocity sensor, a proportional controller can be implemented to realize Direct Velocity Feedback (DVF) [1], [4]. While using a displacement sensor a Positive Position Feedback (PPF) controller can be used to realize additional roll-off [1], [4], [6]. Both topologies are applied to laminated structures [20], [21], [22], and discussed in the next sections.

A voltage amplifier can realize a force actuator which if embedded on the beam operating in d_{31} mode produces a pair of torques M at the piezoelectric ends, proportional to the applied voltage as in Equation 10.

A. Direct Velocity Feedback (DVF)

A current amplifier attached to the piezoelectric enforces short circuit conditions and produces a voltage output that is proportional to current i, and hence, velocity, as shown in Equations 30 and 31. Hence, for the piezoelectric embedded on the beam in d_{31} mode, this specifically realizes a sensor for strain-rate $\Delta\dot{\theta}_i$. An inverting current amplifier could be implemented as shown in Fig. 30.

$$i = g_a \, \Delta\dot{\theta}_i \tag{30}$$

Therefore, the voltage output of the current amplifier is:

$$V_{oi} = -Ri \tag{31}$$

Closed-loop stability of DVF control can be proven by the frequency domain analysis. The collocated transfer function G_{vv} has a phase which varies between 0 and -180 degrees. The current sensor adds a 90 degrees phase which guarantees that Nyquist plot of $sGvv(s)$ never encircle the $(-1 + 0j)$

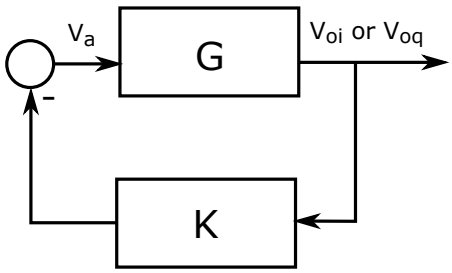

Fig. 29. Control architecture which realizes active damping using different controllers K for different sensor outputs.

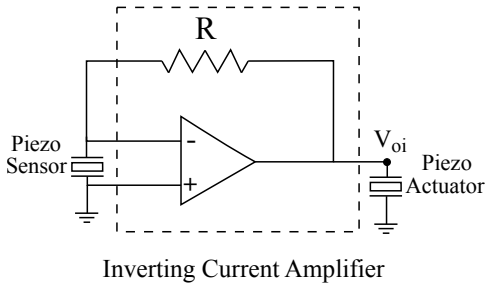

Fig. 30. Schematic of an inverting current amplifier used for achieving Direct Velocity Feedback (DVF).

point in the complex plane. The root locus of the open loop G_{vv} transfer, shows that an additional zero at the origin (i.e., velocity sensor), realizes a locus that is restrained to the left half plane (LHP). Negative feedback of a strictly positive proportional gain g can robustly achieve damping, by shifting the poles along the locus into the LHP.

The damping achieved for the gains $g = [10^4, 10^6]$ is shown in Fig. 33. The gain was tuned to achieve sufficient damping of the scanning motion but also taking the control input into consideration to maintain practical realizability. The magnitude Bode plot shows the damping achieved for the first three modes. Attenuation of scanning motion vibrations is shown in Fig. 34. The control input generated and shown in Fig. 35 has a peak voltage of $20\,V$.

B. Positive Position Feedback (PPF)

Considering the laminated structure which is a distributed parameter system, it doesn't naturally exhibit roll-off at high frequencies [1]. Consequently, the spillover phenomena occurs where unmodelled dynamics contribute to the closed loop system and might cause instability. Although DVF allows for spillover, however, this doesn't cause instability [4]. Positive position feedback (PPF) was introduced in [6], as a controller which is specifically robust against spillover instability. On the other hand, it has to be tuned to target specific modes and the control action is limited to these modes only. The PPF controller is an auxiliary second order system which has the displacement as an input and the control force as an output. The advantageous property is that the frequency response of

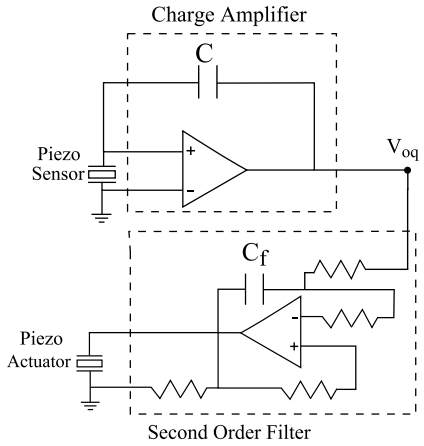

Fig. 32. Schematic of a charge amplifier followed by a second order filter used for achieving Positive Position Feedback (PPF).

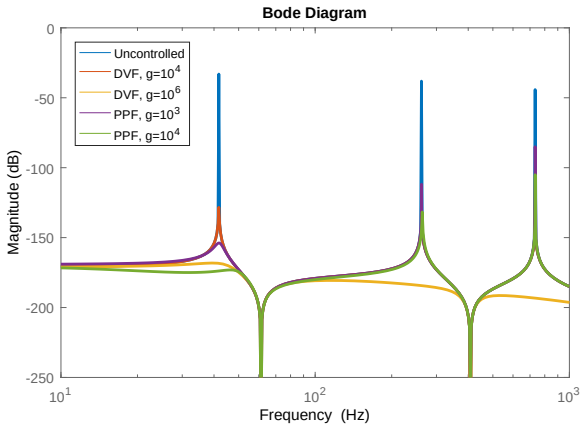

Fig. 33. Magnitude Bode plot of the damped G_{vv} transfer function versus the uncontrolled case, using a Direct Velocity Feedback (DVF) and a Positive Position Feedback (PPF) controllers.

the controller rolls off at high frequencies making it insensitive to the unmodelled high frequency dynamics.

This controller is used with a charge amplifier as shown in Fig. 32, that realizes a displacement sensor, more specifically, a strain sensor. Therefore, the voltage output of the charge amplifier is:

$$V_{oq} = \frac{-Q}{C} \tag{32}$$

Where C is the feedback capacitance.

A second order PPF controller is defined as:

$$K = \frac{-g\,\omega_f^2\,\omega_i^2}{s^2 + 2\zeta_f\omega_f s + \omega_f^2} \tag{33}$$

Where the controller parameter ω_f is tuned to be in the vicinity of the targeted mode ω_i. This controller requires to be tuned to a certain frequency, and accordingly, only achieves damping to the modes close to that frequency. In order to target multiple modes, more than one PPF controller can be used.

The root locus of the open loop $K(s)G_{vv}(s)$ transfer shows that locus is contained in the LHP except for a branch on the positive real axis. Controller roll-off could be observed by

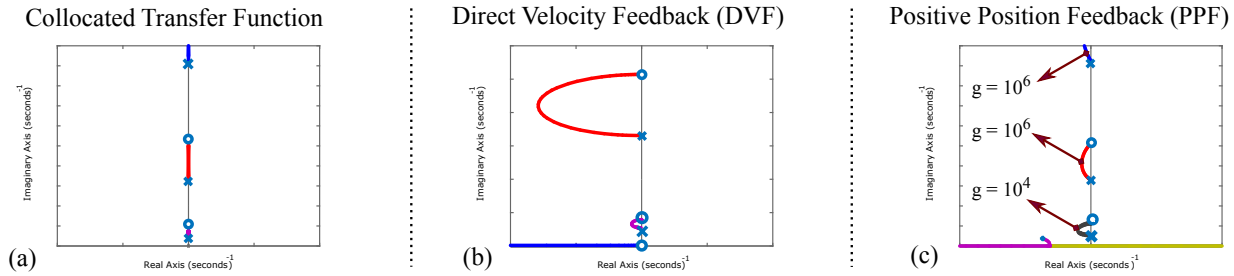

Fig. 31. Root loci of the DVF (b) and PPF (c) controllers applied to the structure embedded with collocated piezoelectric transducers. The alternating pole-zero pattern of the collocated transfer function is shown in (a). The symmetric upper half is shown only.

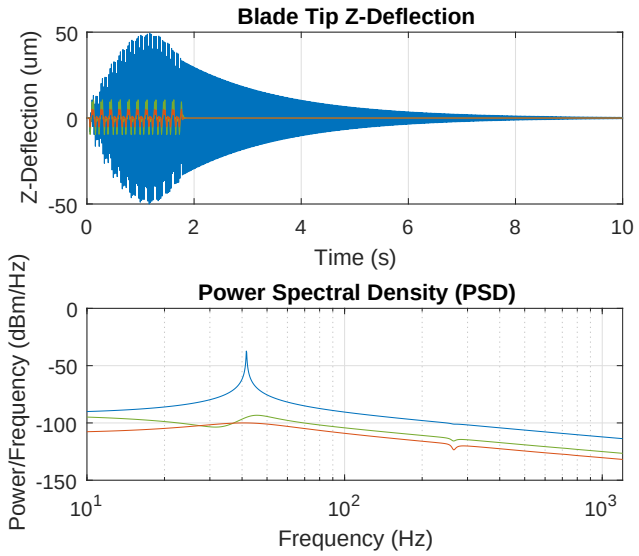

Fig. 34. Simulated spectral analysis of the actively damped blade tipz Z-deflections for scanning motion excitation.

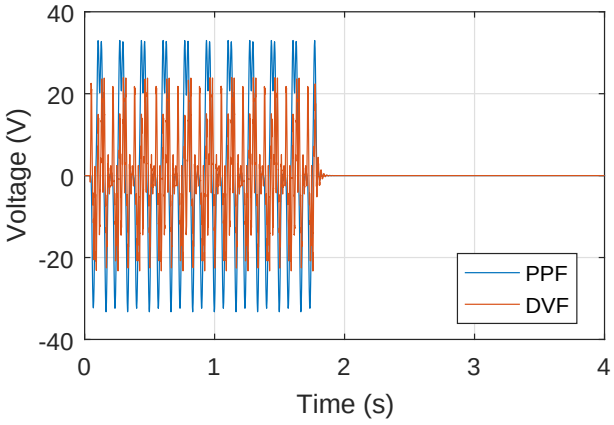

Fig. 35. Control input generated by the DVF and PPF controllers during scanning motion.

increasing the gain where the high frequent poles relative to ω_f move slower than the targeted poles.

Stability of the PPF controller could be analyzed from the characteristic equation of the closed-loop system:

$$\begin{aligned} G_{cl} &= 1 + K(s)G_{vv}(s) \\ &= 1 + \frac{-g}{s^2 + 2\zeta_f\omega_f s + \omega_f^2} \cdot g_a^2 \sum_{i=1}^{3} \frac{\Delta\theta_i^2}{s^2 + \omega_i^2} \\ &= s^2 + 2\zeta_f\omega_f s + \omega_f^2 - g\, g_a^2 \sum_{i=1}^{3} \frac{\Delta\theta_i^2}{s^2 + \omega_i^2} \end{aligned} \tag{34}$$

The system becomes unstable when any of the coefficients of the power expansion of the characteristic equation is negative, according to Routh-Hurwitz criterion. Accordingly, the stability condition can be derived from the condition of the constant term as:

$$\omega_f^2 - g\, g_a^2 \sum_{i=1}^{3} \frac{\Delta\theta_i^2}{\omega_i^2} > 0 \tag{35}$$

This could be reformulated in terms of the controller gain g:

$$g < \frac{\omega_f^2}{g_a^2} \sum_{i=1}^{3} \frac{\omega_i^2}{\Delta\theta_i^2} \tag{36}$$

Alternatively, it could be stated that the stable controller gains g should be less than the inverse of the static loop gain:

$$g < \frac{1}{G_{vv}(0)K(0)} \tag{37}$$

The damping achieved for gains $g = [10^3, 10^4]$, $\zeta_f = 0.9$ and $\omega_f = 41.8\ Hz$ is shown in Fig. 33. The gain was tuned to achieve sufficient damping of the scanning motion in order to optimize stability robustness. The magnitude Bode plot in Fig. 33 and the PSD of the scanning motion in Fig. 34 show the damping achieved. The control input generated is shown in Fig.35 has a peak voltage of $30\ V$.

In conclusion, the performance achieved using both controllers are comparable in the application of damping of the scanning motion. The control input required for the DVF controller is slightly less than the PPF. Robustness analysis is rather qualitative in this case. DVF control is robust against system parameter uncertainties as it is not model based, however one should be careful that in practice a low pass filter is appended, i.e., limited bandwidth current amplifier. Therefore, out of bandwidth modes shouldn't be dominant. On the other hand, stability of PPF control is not affected by sensor/actuator dynamics due to the roll-off. However, it has to be tuned properly to a certain mode, which makes it less robust to variation in the system's natural frequencies.

VI. Self-powered Vibration Control

In this section, self-powered vibration control during scanning motion is presented. Based on the idea of utilizing the source of vibration excitation, i.e., scanning motion, as a source of energy to supply the power needed for vibration damping, self-powering is achieved. The harvested power can be utilized to power a gyrator, and therefore, implement passive shunt damping, or utilized to implement an active damping feedback control topology. This is shown in Fig. 36. Moreover, the harvesting unit could be used to generate a feedforward signal to compensate for vibrations in advance. In this work, the implementation is limited to the simpler case of powering passive shunt damping, due to the fact that the performance achieved is comparable for this application.

A. Scanning Motion Energy Harvester

The scanning motion energy harvester proposed consists of a cantilevered piezo film orthogonal to the scanning direction. A tip mass m_t is attached to the piezo tip in order to reduce its natural frequency relative to the excitation frequency, and hence, increase the strain.

1) Electrical Model: A piezoelectric material could be electrically modeled as a current source I_p in parallel to capacitance C_p as shown in Fig. 37 [12]. This could be derived starting from the constitutive equation of the piezoelectric film:

$$D = e_{31} S + \epsilon_{31}^S E \tag{38}$$

Rewriting this equation in macroscopic variables using the piezo area A, length l, and thickness t, yields:

$$AD = \frac{A}{l} e_{31}\, x_{tip} + \frac{A}{t} \epsilon_{31}^S V_p \tag{39}$$

Where x_{tip} is the tip displacement, and V_p the piezoelectric voltage.

Finally, differentiating derives an equation for the current source value in terms of the tip velocity $\dot{x}_{tip}$:

$$I_p = \theta\, \dot{x}_{tip} + C_p^x\, \dot{V}_p \tag{40}$$

Where,

$$\begin{aligned} C_p^x &= \frac{A}{t}\epsilon_{31}^S = \frac{A}{t}\epsilon_{31}^T(1-k_{31}^2) = C_p^F(1-k_{31}^2), \\ \theta &= \frac{A}{l} e_{31} \end{aligned} \tag{41}$$

2) Mechanical Model: In order to determine the tip relative velocity due to the base excitation of the cantilevered piezoelectric, the transmissibility is derived considering the dominant first mode, due to the tip mass:

$$\frac{\dot{x}_{tip,r}}{\dot{x}_{base}} = \frac{-s^2}{s^2 - 2\zeta\omega_p - \omega_p^2} \tag{42}$$

Where:

$$\omega_p = \sqrt{\frac{k_m}{m_t}} \tag{43}$$

Where k_m and ω_p are the equivalent stiffness and natural frequency of the piezoelectric film, respectively.

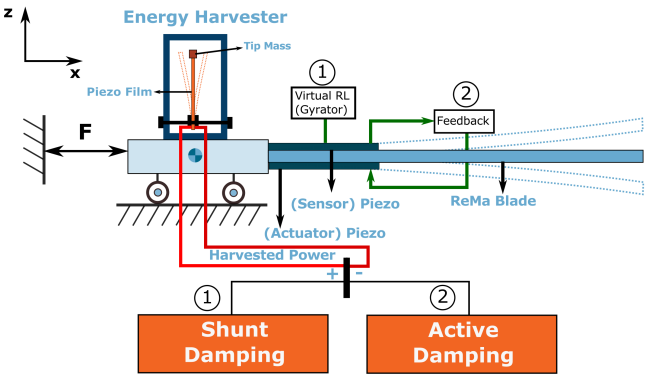

Fig. 36. Passive shunt and active feedback damping could be implemented utilizing the harvested power from scanning motion.

TABLE III
Harvesting Piezo Dimensions and Properties

Parameter	Value	Unit	Parameter	Value	Unit
l_p	46.0	$[mm]$	$-d_{31}, d_{33}$	$320, 650$	$[pC/N]$
b_p	20.8	$[mm]$	$k_{31}, k_{33},$	$0.43, 0.75$	$[\,]$
t	0.18	$[mm]$	k_t	0.55	$[\,]$
C^F	190	$[nF]$	Y_{11}^E, Y_{33}^E	$63, 50$	$[GN/m^2]$
C^x	160	$[nF]$	k_m	573.67	$[N/m]$

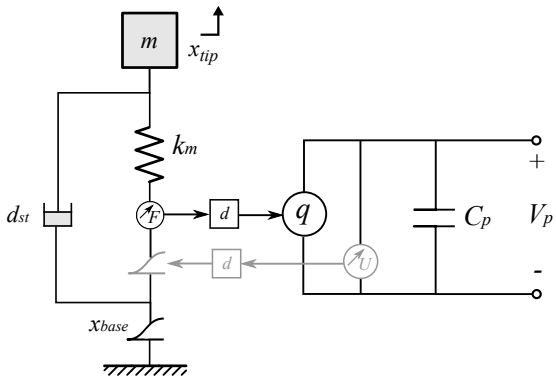

Fig. 37. An equivalent electromechanical model of the cantilevered piezoelectric film with tip mass attached.

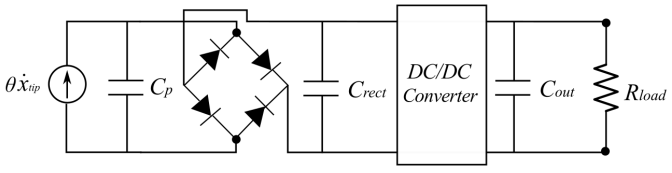

Fig. 38. Energy Harvesting Circuit using a rectifier and step-down DC/DC converter.

A configuration of the harvester has been realized consisting of a $m_t = 5\,g$ tip mass while performing the scanning motion presented previously. The dimensions and material properties of the piezoelectric film used is shown in Table III. Therefore, $\theta = 0.0033, \omega_p = 338.53\,rad/s$ are evaluated accordingly.

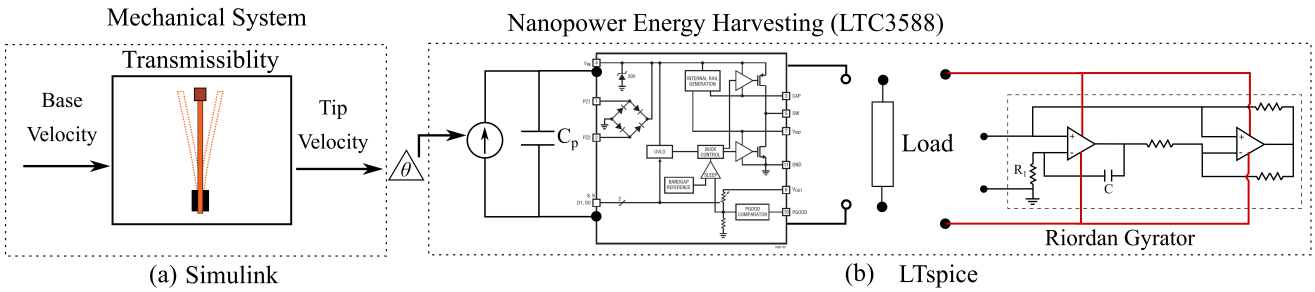

Fig. 39. Simulating the harvesting piezo tip velocity due to the scanning motion excitation using Simulink (a). This is followed by estimating the power output of the energy harvesting circuit using LTspice (b).

B. Energy Harvesting

The vibrating piezoelectric differs from a regular power source in three main aspects, the varying nature of the excitation amplitude and frequency, the output which typically has high voltage and low current, and finally the capacitive nature of the piezo source. Hence, different harvesting circuits that maximize and regulate the power output have been developed [23], [24], [25].

A method which optimizes the harvested power using a step-down DC/DC converter, i.e., buck regulator, is proposed in [23]. A full-wave bridge rectifier with a smoothing capacitor is followed by a step-down DC/DC converter as shown in Fig. 38. This converter regulates the flow of energy from the piezoelectric element to the desired load, allowing for changing the output voltage of the rectifier as the mechanical excitation changes to achieve and maintain the maximum power flow. The converter is inherently designed, using internal feedback, to maximize the power flow. Therefore, this results in the piezoelectric harvesting maximum power. Additionally, the step-down converter regulates the rectifier output from a high voltage low current one, to a lower voltage but higher current suitable for electronic loads. An important aspect for the converter is to be with high efficiency but also low quiescent current to allow for its self-powering. An integrated solution with further optimization and additional features is offered in the LTC3588 integrated circuit.

A two step simulation procedure is performed as shown in Fig. 39 using Simulink and LTSpice. Using Simulink, the piezo tip displacement and velocity due to the scanning motion is simulated and shown in Fig. 40. A displacement of $1\ mm$ and a current amplitude of $0.48\ mA$ are expected.

Using the relation in equation 40, the output current of the piezo could be modeled as a current source in the LTSpice simulation using the piezo tip velocity derived previously. Hence, the rectifier and the converter outputs are shown in Fig. 41 and Fig. 42, respectively. The rectifier has a high voltage output of $40V$ at $1M\Omega$ load, which drops to $30V$ for a $300k\Omega$ load. The converter regulates this to $4.2\,V$ with higher current flowing continuously through an $8k\Omega$ load. This estimates a power output of $2.2\ mW$.

Increasing the power output could be performed by maximizing the tip mass and further lowering the natural frequency of the piezo to the excitation frequency. A tip mass of $25\ g$ could generate a power output up to $34\ mW$ [26].

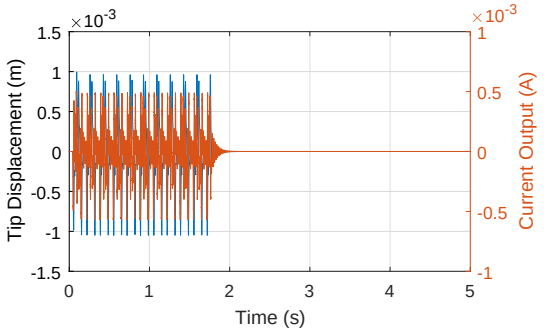

Fig. 40. Harvesting piezo tip displacement and current output (i.e., $\theta\times$ tip velocity) with tip mass of $5\,g$ during scanning motion excitation (Simulation).

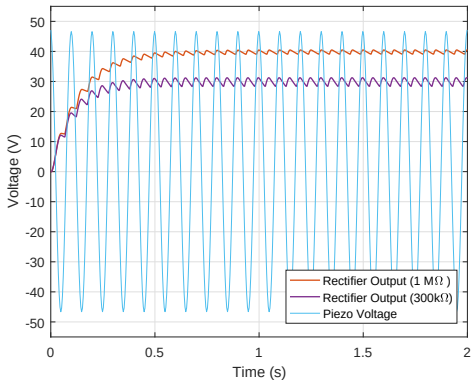

Fig. 41. Rectifier high DC voltage output during scanning motion (Simulation).

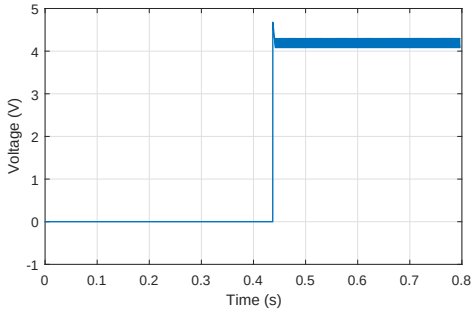

Fig. 42. Step-down converter low voltage output with current flowing through a $8k\Omega$ load (Simulation).

VII. Experimental Results

In this section, the proposed solutions are validated through experimentation on a photolithography reticle masking test-rig. The experimental setup in Fig. 6 has been used to validate the effectiveness of the previously designed approaches. Firstly passive and active damping are demonstrated using external power, then the self-powered approach is presented.

A. Passive Damping

The designed RL circuit is used to shunt the embedded piezo on the blade in this section. A Riordan gyrator is implemented using LM324 Quad op-amp to simulate the required inductance. The estimated FRF of the implemented gyrator is shown in Appendix III-B.

One piezo is excited with the sine sweep and the G_{yv} transfer is estimated, while shunting the other piezo with the RL circuit. The FRF is shown in Fig.45, while the time response in Fig. 49. Similarly, the actuator piezo is excited with a white noise signal and the time response is shown in Fig. 46. Different tuning values for the gyrator capacitor and shunt resistance are shown in Fig.'s 43 and 44.

The optimal values for the RL shunt $(7\,\mu F,\ 11.5\,k\Omega)$ are fine tuned relative to the design values of $(7.28\mu F,\ 12.08\,k\Omega)$. The damped G_{yv} transfer shows $13\,dB$ of damping achieved through RL shunting matching the expected value of $14\,dB$ in simulation. In the time domain, a sine sweep excitation is damped from peak amplitude of $37.5\ \mu m$ to $18\ \mu m$. White noise excitation is damped from peak amplitude of $7.7\ \mu m$ to $4.1\ \mu m$ relative to the background noise with peak amplitude of $1.9\ \mu m$.

Similarly, the step and scanning motion excitations are damped showing a settling time reduction to $1\ s$ from $4\ s$ and $6\ s$ for step and scanning motions, respectively. The peak amplitude after the excitation shows a reduction from $47\mu m$ to $13\mu m$ for scanning motion. The spectral analysis validates that the reduction is achieved due to the dominant mode attenuation of $65\ dBm/Hz$.

B. Power Aspects

The power required by the Riordan gyrator composed from two op-amps is measured in this section. This analysis is specific for the type of the op-amp used, LM324 in this case. The current is measured by means of the voltage drop across a shunt resistor. The supply voltage required for damping scanning motion should not be less than the piezo voltage output during excitation to reach optimal performance. A supply voltage of $5\,V$ is considered.

The current flow is dependent on the supply voltage as shown in the LTSpice simulations in Fig. 48. For $10\,V$ supply voltage the current flow is measured experimentally to be around $0.705\ mA$ as shown in Fig. 51. For a supply voltage of $5\,V$ the current consumed is around $0.38\ mA$. Therefore the power required could be calculated as:

$$\begin{aligned} P &= V\,I \\ &= 5 \times 0.38 = 1.9\,mW \end{aligned} \tag{44}$$

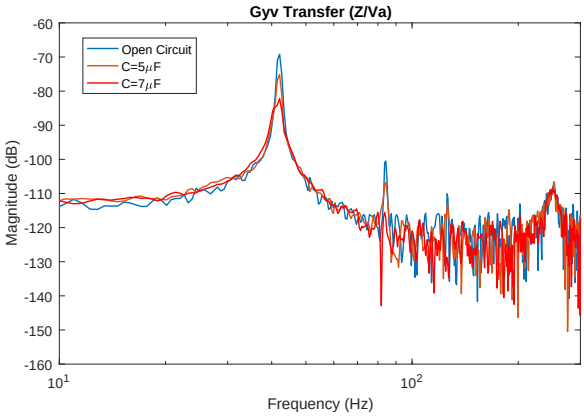

Fig. 43. Varying the capacitance shows the tuned $7\mu F$ versus detuned values. Resistance of $10\ k\Omega$ was used.

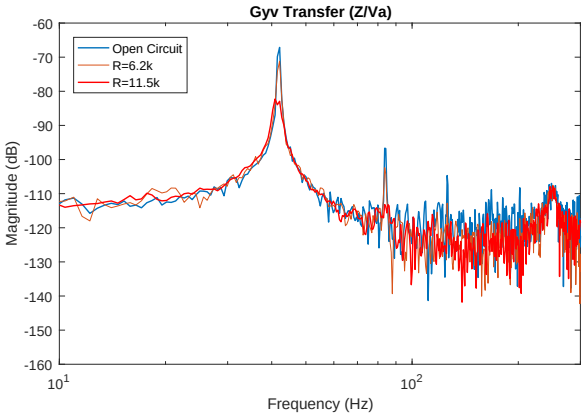

Fig. 44. Varying the resistance with the tuned capacitor of $7\ \mu F$ shows the optimal value of $R = 11.5\ k\Omega$.

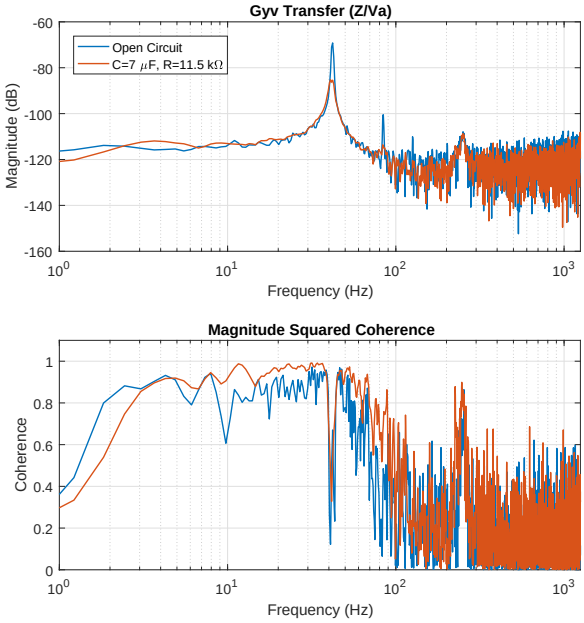

Fig. 45. Optimally tuned RL shunt with capacitance of $7\,\mu F$ and resistance of $11.5\ k\Omega$.

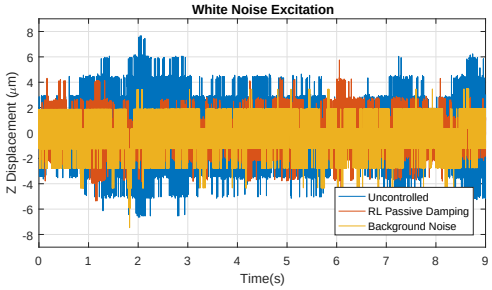

Fig. 46. Time response of the blade Z displacement during white noise piezo excitation.

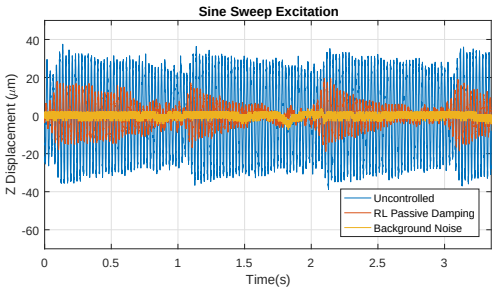

Fig. 49. Time response of the blade Z displacement during sine sweep piezo excitation.

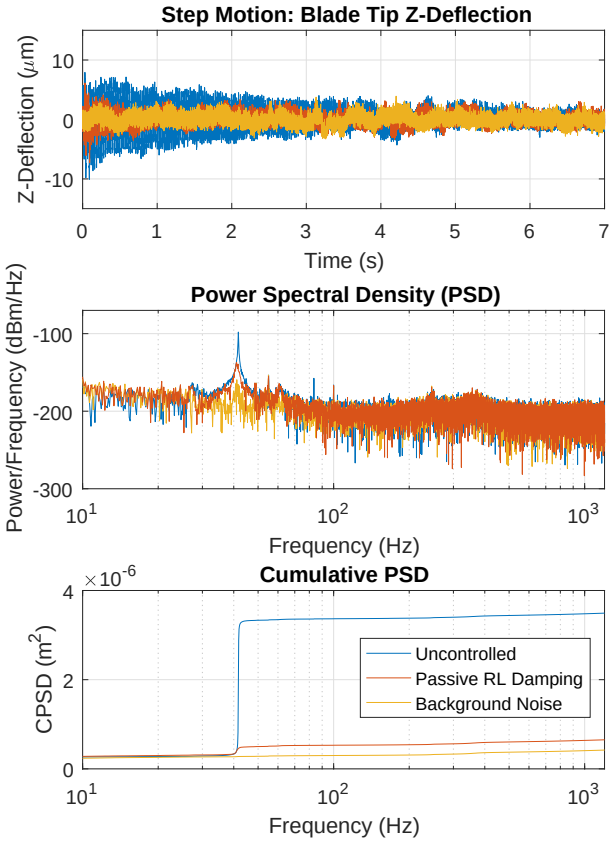

Fig. 47. Experimental spectral analysis of the passive damped blade tip Z vibrations for step motion excitation.

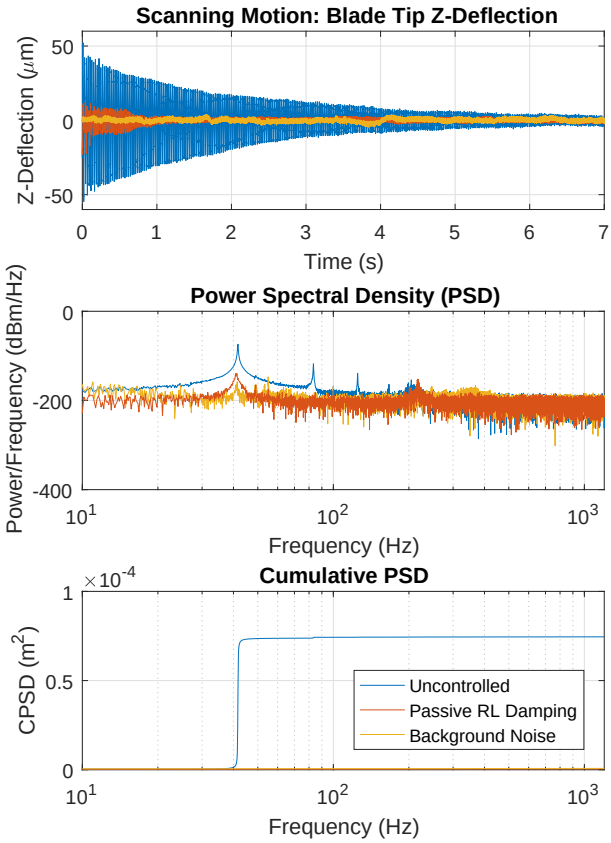

Fig. 50. Experimental spectral analysis of the passively damped blade tip Z vibrations for scanning motion excitation.

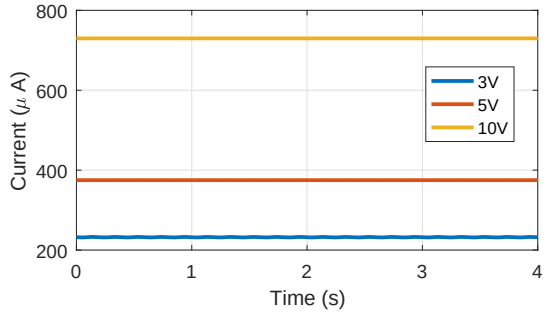

Fig. 48. Current flow through the gyrator supply using different supply voltages (Simulation).

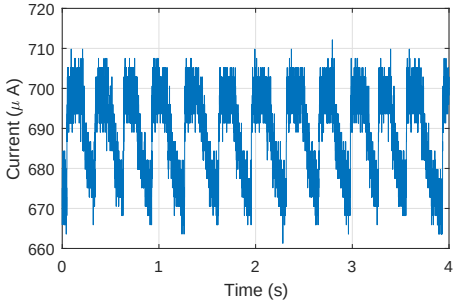

Fig. 51. Current flow through the gyrator during scanning with $10\,V$ supply voltage (Experimental).

C. Active Damping

Active damping using piezoelectric materials is validated in this section. A Direct Velocity Feedback controller is implemented using an inverting current amplifier with a $1\,M\Omega$ feedback resistance, followed by a low pass filter to limit the bandwidth of the differential action. The controller output is fed into a $10x$ voltage amplifier which drives the piezoelectric actuator.

Stability is checked first by estimating the frequency response of the open loop transfer function $G(s)K(s)$ as shown in Fig. 52. By adding 90 degrees phase from the velocity sensor, i.e., current amplifier, to the plant with phase of 0 and -180 degrees, it could be seen that the open loop transfer function achieves a phase of 90 to -90 degrees and hence stable in closed loop.

Scanning motion excitation is accordingly damped showing a settling time of less than $1\,s$. The spectral analysis validates that the reduction is achieved due to the dominant mode attenuation of around $70\,dBm/Hz$.

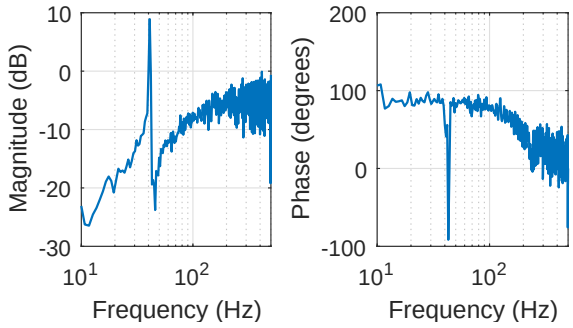

Fig. 52. Stability check by estimating the frequency response of the open loop transfer function with the Direct Velocity Feedback controller. The phase ranges from 90 to -90 degrees due to the added phase of the velocity sensor.

D. Self-Powered Vibration Control

The configuration of the clamped harvesting piezo with a $5\,g$ tip mass attached is realized as shown in Fig. 55. The power output could be further optimized by increasing the tip mass within the safe limits of the piezo.

The harvesting piezo output is rectified using a full wave bridge rectifier followed by a $10\,\mu F$ smoothing capacitor. The voltage output of the piezo during scanning motion is shown in Fig. 56 for no load ($1\,M\Omega$ scope resistance), and in Fig. 57 for a $300\,k\Omega$ load. This is measured to be $40\,V$ peak voltage, and $25\,V$ DC voltage for both cases, respectively. Hence, this estimates a power output of $2.1\,mW$.

Following the rectification is a buck regulator (DC/DC converter) in order to regulate the output to a certain desired voltage in addition to matching the input impedance such that maximum power is harvested, thus optimize efficiency. The low voltage/high current output of the high efficiency buck regulator during scanning for a 500Ω load is shown in Fig. 58. This estimates a power output of $2\,mW$.

Another quantitative way to asses the feasibility of the self-powered vibration control is the time required to charge a storage element, i.e., capacitor C_r, by scanning with no load. Hence, a storage element could serve as a reservoir to provide enough energy for damping step motion. Fig. 58 shows that it takes $600\,ms$ for charging a $1\,mF$ capacitor to $1.8\,V$, while approximately $100\,ms$ is needed for a $100\,\mu F$ capacitor. Accordingly, the time of discharging into a resistive load R_{load} is determined by $\tau = R_{load}C_r$.

Finally, self-powered passive shunting is realized through the scanning motion energy harvester powering the gyrator. The vibrations were attenuated from $15.7\,\mu m$ to $6.7\,\mu m$ due to the dominant mode attenuation of $25dbm/Hz$ as shown in Fig. 59. For self-powering of an active damping solution, integrated circuit amplifiers with low power consumption and capability of driving the capacitive piezo load have to be designed.

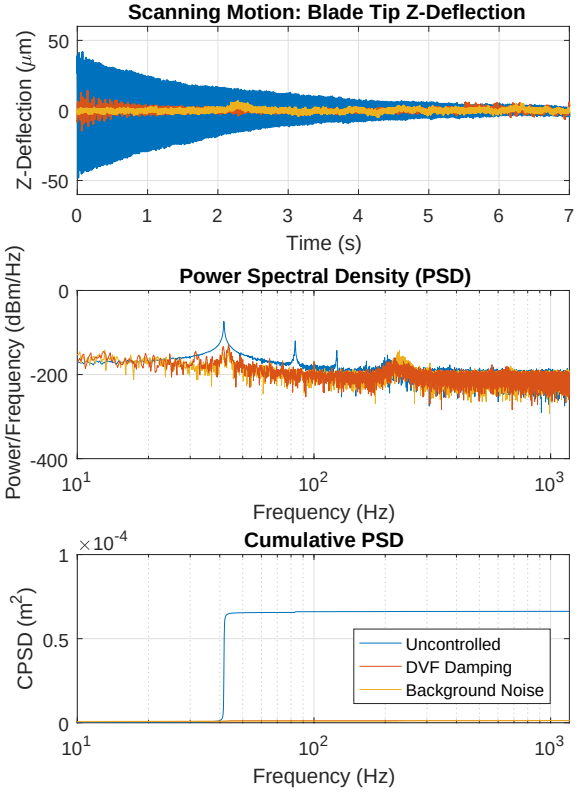

Fig. 53. Experimental spectral analysis of the actively damped blade tip Z-deflections after scanning motion excitation.

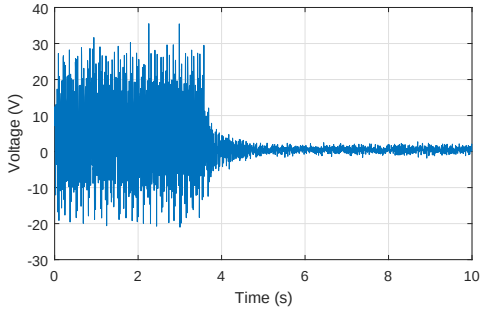

Fig. 54. DVF control effort generated during scanning.

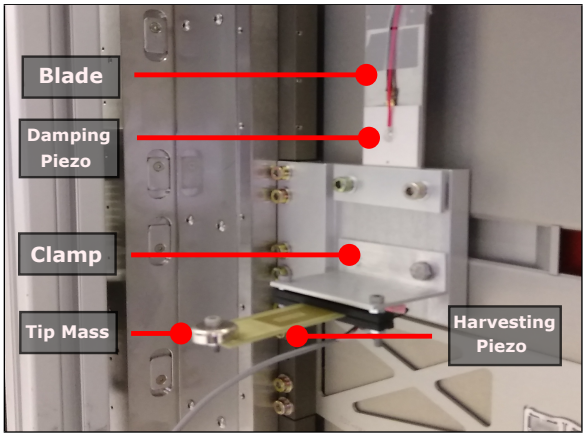

Fig. 55. Photo of the piezo harvesting unit consisting of a cantilevered piezoelectric film with a tip mass attached to the mover orthogonal to the scanning motion direction.

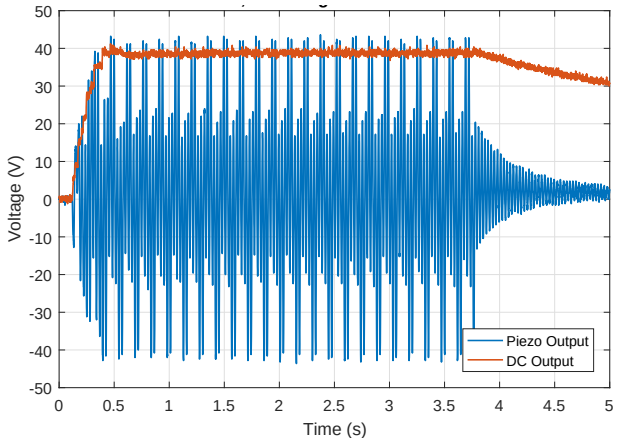

Fig. 56. No electrical load ($1 M\Omega$ scope resistance) harvesting piezo voltage output during scanning motion versus the DC output after rectification and smoothing.

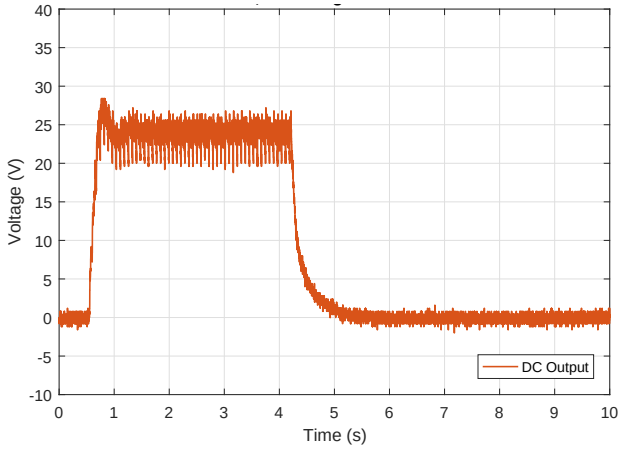

Fig. 57. Rectifier DC voltage output during scanning with a $300\,k\Omega$ resistive load.

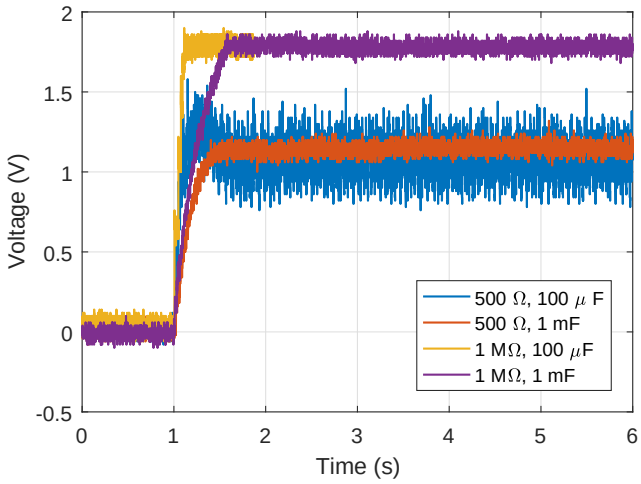

Fig. 58. Buck regulator low voltage/high current output for a $500\,\Omega$ and no load conditions during scanning for different smoothing capacitors.

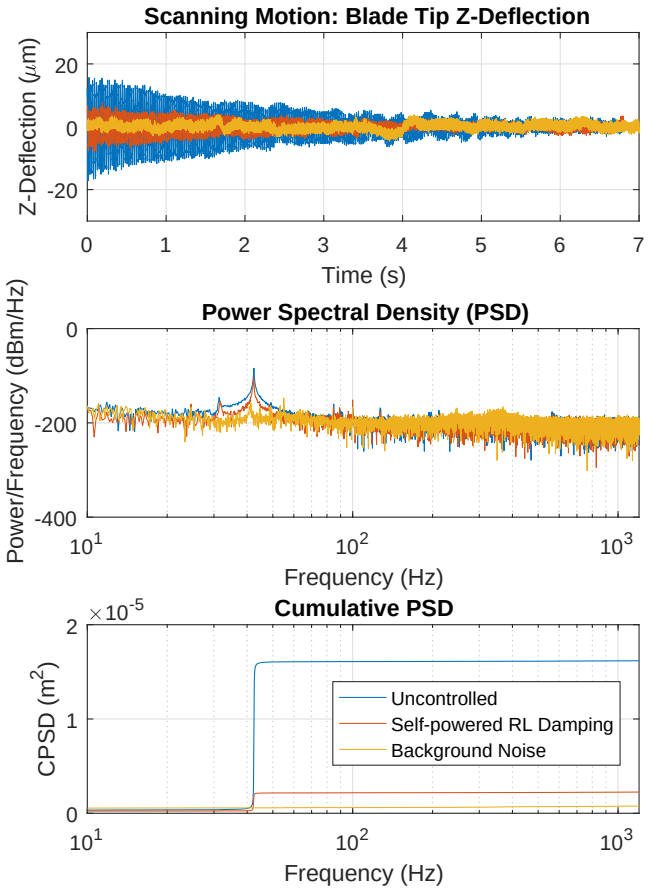

Fig. 59. Experimental spectral analysis of the self-powered RL damped blade tip Z vibrations for scanning motion excitation.

VIII. Conclusion

In this paper, a self-powered vibration control solution using piezoelectric materials that is applicable to the low level vibrations within a high precision application was proposed. This was successfully achieved using a scanning motion energy harvester which provides power for a suitable vibration damping solution. A passive shunting and active feedback controllers have been designed as possible vibration control approaches. The first approach is RL passive shunting, while the second are the Direct Velocity Feedback and Positive Position Feedback controllers. The scanning motion energy harvester was designed as a cantilevered piezoelectric film with a tip mass such that enough power is supplied for realizing simulated inductors. The proposed approaches were validated experimentally through damping the vibrations of the reticle masking blades within a photolithography machine due to scanning motion excitation. An attenuation of 57% of the vibration peak amplitude has been achieved through self-powered damping of the dominant mode.

Acknowledgment

The authors would like to thank ASML B.V., Netherlands, for providing its facilities for this research.

References

[1] A. Preumont, *Vibration Control of Active Structures, An Introduction*. Springer, 2011.

[2] S. B. Chikkamaranahalli, R. R. Vallance, B. N. Damazo, and R. M. Silver, "Damping mechanisms for precision applications in ultra high vacuum environment," *American Society for Precision Engineering*, 2006.

[3] N. Hagood and A. von Flotow, "Damping of structural vibrations with piezoelectric materials and passive electrical networks," *Journal of Sound and Vibration*, 1991.

[4] S. R. Moheimmani and A. J. Fleming, *Piezoelectric Transducers for Vibration Control and Damping*. Springer, 2006.

[5] R. Riordan, "Simulated inductors using differential amplifiers," *Electronic Letters, Vol. 3*, 1967.

[6] J. L. Fanson and T. K. Caughey, "Positive position feedback-control for large space structures," *AIAA Journal*, 1990.

[7] J. J. Dosch and D. Inman, "A self-sensing piezoelectric actuator for collocated control," *Intelligent Materials, Systems, and Structures*, 1992.

[8] D. Niederberger and M. Morari, *Smart Damping Materials using Shunt Control*. PhD thesis, Swiss Federal Institute of Technology (ETH), 2005.

[9] M. Konak and I. Powlesland, "A self-powered discrete time piezoelectric vibration damper," in *SPIE Smart Materials, Structures, and MEMS*, 2000.

[10] Z. Wang and L. Gaudiller, *Enhanced Self-powered Vibration Damping of Smart Structures by Modal Energy Transfer*. PhD thesis, Linstitut national des sciences appliques de Lyon, 2015.

[11] *ASML, B.V. on https://www.asml.com*.

[12] J. Holterman and P. Groen, *An introduction to Piezoelectric Materials and Applications*. Applied Piezo, 2013.

[13] Y. Liao and H. Sodano, "Optimal placement of piezoelectric material on a cantilever beam for maximum piezoelectric damping and power harvesting efficiency," in *Smart Materials and Structures*, 2012.

[14] J. Holterman and T. J. de Vries, "Active and passive damping based on piezoelectric elements, controllability issues," *Workshop on European Scientific and Industrial Collaboration*, 2001.

[15] A. A. Eielsen and A. J. Fleming, "Passive shunt damping of a piezoelectric stack nanopositioner," *American Control Conference*, 2010.

[16] B. Mokrani, R. Bastaits, R. Viguie, and A. Preumont, "Vibration damping of turbomachinery components with piezoelectric transducers: Theory and experiment," *Proceedings of ISMA*, 2012.

[17] M. V. Kozlowski, D. G. Cole, and R. L. Clark, "A comprehensive study of the rl series resonant shunted piezoelectric: A feedback controls perspective," *Vibrations and Acoustics*, 2011.

[18] P. Akella, X. Chen, W. Cheng, D. Hughes, and J. T. Wen, "Modeling and control of smart structures with bonded piezoelectric sensors and actuators," *Smart Materials and Structures*, 1994.

[19] J. Holterman and T. J. de Vries, "Active damping within an advanced microlithography system using piezoelectric smart discs," *IEEE Transactions on Mechatronics*, 2004.

[20] A. E. Badawy and M. E. Masry, "Positive position feedback active vibration control of a smart cantilever beam using ansys," in *International Conference of Electrical, Automation and Mechanical Engineering*, 2015.

[21] M. J. Balas, "Direct velocity feedback control of large space structures," *Journal of Guidance, Control, and Dynamics*, 1979.

[22] H. Yamada, M. Sasaki, and Y. Nam, "Active vibration control of a microactuator for hard disk drives using self-sensing actuator," *Journal of Intelligent Materials Systems and Structures*, 2008.

[23] G. K. Ottman, H. F. Hofmann, and G. A. Lesieutre, "Optimized piezoelectric energy harvesting circuit using step-down converter in discontinuous conduction mode," *IEEE Transactions on Power Electronics*, 2003.

[24] A. F. G.-C. Espinosa, A. S. Ramirez, L. F. C. Alfonso, R. Loendersloot, and A. Berkhoff, "Development of a piezoelectric based energy harvesting system for autonomous wireless sensor nodes," in *European Workshop on Structural Health Monitoring*, 2014.

[25] F. S.Souza, N. Oki, J. V. Filho, R. Loendersloot, and A. P. Berkhoff, "Accuracy and multi domain piezoelectric power harvesting model using vhdl-ams and spice," in *IEEE Sensors*, 2016.

[26] *Mide, Engineering Smart Technology Products on http://www.mide.com*.

Samer Abdelmoeti received the B.Sc. degree in Mechatronics Engineering from the German University in Cairo, Cairo, Egypt, in 2015. He is currently working towards the M.Sc. degree in Robotics and Mechatronics at the University of Twente, Enschede, The Netherlands. His research interests include motion and vibration control, real time control, robotics and mechatronics.

Bas Jansen received his B.Eng. degree in Mechanical Engineering from the University of Applied Sciences, Utrecht, The Netherlands, in 2002 and his M.Sc. degree in Mechatronics from Delft University of Technology in 2010, Delft, The Netherlands. From 2007 onwards he is working at ASML Veldhoven, The Netherlands. His main research interests are modeling and control of high precision piezo actuated systems.

Theo J.A. de Vries (M96) was born in Wolvega, The Netherlands, in 1966. He received the M.Sc. and Ph.D. degrees in electrical engineering from the University of Twente, Enschede, The Netherlands, in 1990 and 1994, respectively, following a special program that combined courses of the Faculties of Electrical Engineering and Mechanical Engineering. From 1994 to 1999, he was an Assistant Professor, and since 1999, he has been an Associate Professor of intelligent control and mechatronics at the Control Laboratory, University of Twente. In 2001, he co-founded Imotec B.V., Hengelo, The Netherlands, a mechatronic engineering and development company, and has operated as CTO for this company since then. His main research interest is the development of controlled electromechanical systems using learning controllers.

APPENDIX I
SYSTEM MODELING

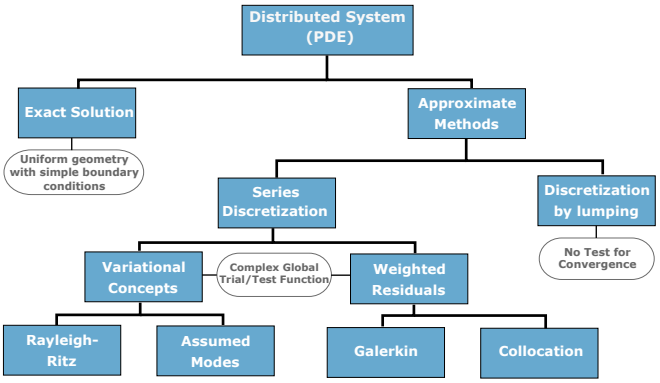

Fig. 60. Exact and approximate solutions to distributed parameter systems.

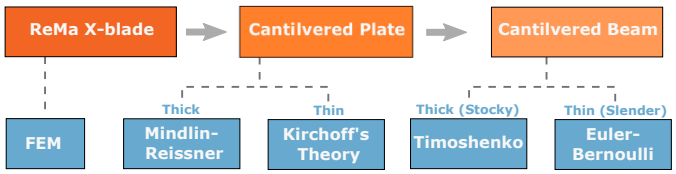

Fig. 61. Existing theories for modelling the ReMa X-blade.

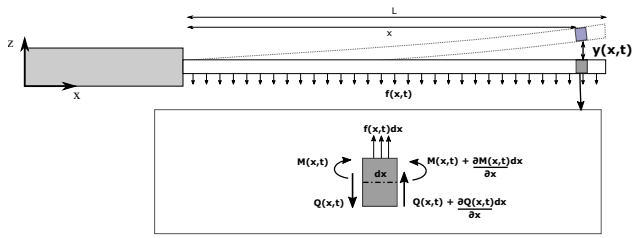

Fig. 62. Free body diagram of a beam element in bending vibration.

A. Structural Vibrations

In a typical vibration problem, flexibility is usually modeled using an intuitive or systematic method. The intuitive method is limited to systems where the flexibility can be derived using model reduction based on the elimination of mass and stiffness elements according to the intuition of the physical problem. Systematic methods treat the structure as a distributed system, thus the mass and elasticity are considered as distributed or continuous parameters. The vibration problem of distributed systems is either solved analytically reaching an exact solution or by approximate methods. Exact solutions are limited to ideal structures (uniform geometry and material properties) with simple boundary conditions. Approximate methods offer solutions to more complex structures with various boundary conditions. These methods are based either on series discretization or discretization by lumping.

Discretization by lumping aims to discretizing the structure into n masses connected by springs. Accordingly, n Ordinary Differential Equations (ODEs) are solved through algebraic eigenvalue problems, as the model is time dependent only. This method has no test for convergence, i.e., no indication for the appropriate number of n which accurately represents the flexibility of the structure. Series discretization treats the structure rather as a distributed system which is time and space dependent. Therefore, a Partial Differential Equation (PDE) has to be solved, through a differential eigenvalue problem. Discretization is based either on variational concepts such as Rayleigh-Ritz and Assumed Modes or weighted residuals such as Galerkin and Collocation. On the other hand, Finite-Element-Methods (FEM) divides the structure into elements (meshing), and then each element is solved through series discretization, however, in this case the element has a simple structure for which a test function can be easily derived using a low order polynomial. Fig. 60 shows the path on how to approach a vibration problem considering different methods.

In this problem, the ReMa X-blade is considered a cantilevered plate as a general case. There exist well established theories through which one could find the solution for this type of geometry and boundary conditions. Kirchoff's theory could be applied for a thin plate assumption, while Mindlin-Reissner theory extends it to thick plates. Similarly, an Euler Bernoulli beam is based on a thin (slender) beam assumption, while Timoshenko's is for a thick (stocky) beam.

Fig. 61 shows the different theories for modelling the ReMa X-blade.

B. Euler-Bernoulli Beam

Bending vibrations of the ReMa X-blade are solved in this section based on the Euler-Bernoulli cantilevered beam assumption.

Fig. 62 shows a uniform beam with an infinitesimal element of width dx. The Newton-Euler dynamical equations of motion are then derived for this element.

Considering $m(x)$ and $EI(x)$ as the mass and flexural rigidity both per unit length, respectively, the force and moment equations are formulated.

Force Equation:

$$Q(x,t) + \frac{\partial Q(x,t)}{\partial x}dx - Q(x,t) + f(x,t)dx = m(x)dx\,\frac{\partial^2 y(x,t)}{\partial t^2} \tag{45}$$

By cancelling opposite shear forces, it simplifies into:

$$\frac{\partial Q(x,t)}{\partial x} + f(x,t) = m(x)\,\frac{\partial^2 y(x,t)}{\partial t^2} \tag{46}$$

Moment Equation:

$$-M(x,t) + [M(x,t) + \frac{\partial M}{\partial x}dx] + [Q(x,t) + \frac{\partial Q(x,t)}{\partial x}dx]dx + f(x,t)dx\frac{dx}{2} = 0 \tag{47}$$

It is assumed that the element has negligible product of mass moment of inertia and angular acceleration $I\alpha$.
Ignoring higher order derivatives simplifies Eq. 47 into:

$$\frac{\partial M(x,t)}{\partial x}dx + Q(x,t)dx = 0 \tag{48}$$

Therefore,

$$Q(x,t) = -\frac{\partial M(x,t)}{\partial x} \tag{49}$$

By substituting Eq. 49 in the force Eq. 46 yields:

$$-\frac{\partial^2 M(x,t)}{\partial x^2} + f(x,t) = m(x)\frac{\partial^2 y(x,t)}{\partial t^2} \tag{50}$$

Using the following relation between the bending displacement and bending moment from the mechanics of materials:

$$M(x,t) = EI(x)\frac{\partial^2 y(x,t)}{\partial x^2}, \tag{51}$$

yields the PDE of a general Euler-Bernoulli beam:

$$-\frac{\partial^2}{\partial x^2}[EI(x)\frac{\partial^2 y(x,t)}{\partial x^2}] + f(x,t) = m(x)\frac{\partial^2 y(x,t)}{\partial t^2} \tag{52}$$

Which is a fourth order PDE that is space and time dependent. Solving this equation results in a solution for the deflection $y(x,t)$ which can be evaluated at a certain position x over the length of the beam at time instant t.

Since this PDE is a separable one, an exact solution might be derived using the Separation of Variables principle as follows. Assuming a solution for $y(x,t)$ in the form of:

$$y(x,t) = Y(x)F(t) \tag{53}$$

Inserting this solution into the PDE in Eq. 52:

$$-F(t)\frac{d^2}{dx^2}[EI(x)\frac{d^2Y(x)}{dx^2}] = Y(x)m(x)\frac{d^2F(t)}{dt^2} \tag{54}$$

By separating the time and space variables:

$$-\frac{1}{m(x)Y(x)}\frac{d^2}{dx^2}[EI(x)\frac{d^2Y(x)}{dx^2}] = \frac{1}{F(t)}\frac{d^2F(t)}{dt^2} = \lambda \tag{55}$$

Using the fact that the quantities in Eq. 55 are real, both sides are equal to a constant denoted by λ. Considering the exponential form of the solution of the RHS of Eq. 55: $F(t) = Ae^{st}$, therefore $\lambda = -\omega^2$, where ω is the eigenvalue (modal frequency later).

Additionally, assuming the beam has uniform mass per unit length $m(x) = m$, and uniform flexural rigidity $EI(x) = EI$, the LHS of Eq. 55 then becomes:

$$EI\frac{d^4Y(x)}{dx^4} = mY(x)\omega^2 \tag{56}$$

Rearranging yields the Differential Eigenvalue Problem:

$$\frac{d^4Y(x)}{dx^4} - \beta^4 Y(x) = 0, \tag{57}$$

where $\beta^4 = \frac{\omega^2 m}{EI}$.

1) Boundary Conditions: The BVP is solved in this section through specifying two boundary conditions at each end (4th order PDE) of the cantilevered beam.

Fixed End at $x = 0$:

$$\begin{aligned} y(x,t) &= 0 \\ \frac{\partial y(x,t)}{\partial x} &= 0 \end{aligned} \tag{58}$$

Free end at $x = L$:

$$\begin{aligned} M(x,t) = EI(x)\frac{\partial^2 y(x,t)}{\partial x^2} &= 0 \\ Q(x,t) = -\frac{\partial}{\partial x}[EI(x)\frac{\partial^2 y(x,t)}{\partial x^2}] &= 0 \end{aligned} \tag{59}$$

By using the solution of the method of separation of variables in Eq. 53, the boundary conditions can be written as:

$$\begin{aligned} Y(x) = 0, \frac{dY(x)}{dx} &= 0 \\ \frac{d^2Y(x)}{dx^2}, \frac{d^3Y(x)}{dx^3} & \end{aligned} \tag{60}$$

Considering the general solution of Eq. 57:

$$Y(x) = A\sin(\beta x) + B\cos(\beta x) + C\sinh(\beta x) + D\cosh(\beta x) \tag{61}$$

Hence, the boundary conditions are substituted to solve for the constants $A, B, C,$ and D.

First boundary condition yields:

$$\begin{aligned} Y(0) = B + D &= 0 \\ B &= -D \end{aligned} \tag{62}$$

Second boundary condition yields:

$$C = -A \tag{63}$$

Which reduces the general solution into:

$$A(\sin(\beta x) - \sinh(\beta x)) + B(\cos(\beta x) - \cosh(\beta x)) \tag{64}$$

The third and fourth boundary conditions yield the equations:

$$B = -\frac{\sin(\beta L) + \sinh(\beta L)}{\cos(\beta L) + \cosh(\beta L)}A \tag{65}$$

$$cos(\beta L)cosh(\beta L) = -1 \tag{66}$$

Eq. 66 is a transcendental equation which must be solved numerically, however accurate solutions can be obtained through MATLAB. This doesn't violate the fact that this is an exact solution in contrast to the approximate methods. Solving Eq. 66 yields different $\beta_r L$ values, where $r = 1, 2, ..., n$.

Finally, the general equation for the mode shapes is derived from substituting Eq. 65 in Eq. 64:

$$\begin{aligned} Y_r(x) = A_r[\sin(\beta_r x) - \sinh(\beta_r x) - \\ \frac{\sin(\beta_r L) + \sinh(\beta_r L)}{\cos(\beta_r L)}(\cos(\beta_r x) - \cosh(\beta_r x))] \end{aligned} \tag{67}$$

Where A_r normalizes the eigenvectors/mode shapes.

2) Orthonormality: The eigenvectors are said to be orthogonal if the Mass M and Stiffness K matrices are symmetric, resulting in the following relation:

$$\int_0^L m(x)Y_r(x)Y_s(x)dx = 0, \omega_r \neq \omega_s \tag{68}$$

The orthogonality of the natural modes is a guaranteed result to the solution of boundary-value problems. Accordingly, the natural modes obtained in Eq. 67 are already orthogonal. Normalized orthogonal modes are said to be orthonormal.

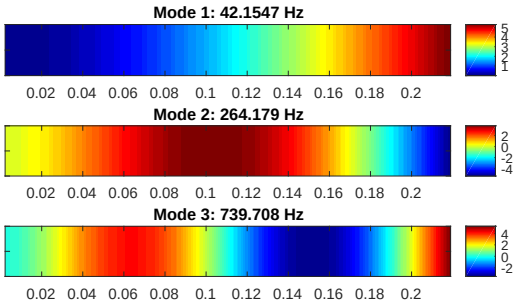

Fig. 63. First three bending modes of the ReMa X-blade using the Euler-Bernoulli beam model.

The natural modes obtained in 67 are then normalized with respect to the mass and stiffness matrices using the following normalization scheme to obtain the normal modes:

$$\int_0^L m(x)Y_r(x)^2dx = 1 \tag{69}$$

Normalization is performed by adjusting the constant A_r of each natural mode. Which yields the advantageous relation:

$$\int_0^L Y_r(x)\frac{d^2}{dx^2}[EI(x)\frac{d^2Y_r(x)}{dx^2}]dx = \omega_r^2 \tag{70}$$

The orthonormality relations allows the representation of the bending displacement in terms of the expansion theorem, which results in the set of modal equations:

$$\ddot{\eta_r}(t) + \omega_r^2\eta_r(t) = 0 \tag{71}$$

Where $\eta_r(t)$ denotes the modal coordinates.

3) Modes and Mode Shapes: In this section, the bending modes and mode shapes are evaluated for the ReMa X-blade using the Euler-Bernoulli beam model derived above. The modal frequencies are calculated using Eq. 57:

$$\omega_r = \sqrt{\frac{EI}{L^4m}}(\beta_r L)^2 \tag{72}$$

Where m is the mass per unit length. The first 3 modal frequencies and corresponding normal mode shapes are presented in Fig. 63.

C. Slenderness Ratio

In order to determine whether or not to consider the thickness of the beam, there exists a deterministic factor called the Slenderness Ratio. Based on this ratio, one could anticipate the magnitude of the error in deflection which results due to considering the simpler assumption, e.g., thin plate/beam.

Firstly, it is worth noting that the thin assumption means that the shear between the top and bottom surfaces of the beam/plate is neglected, where there exists no deformation across the thickness. For a thick structure this assumption is not valid since the structural element is not perpendicular to the bending line anymore, where shear deformation is present.

The Slenderness Ratio is calculated using the length and thickness of the structures, as well as its moduli of elasiticity and moment of inertia, as follows:

TABLE IV
CORRESPONDING ERROR IN DEFLECTION ACCORDING TO THE SLENDERNESS RATIO

Slenderness Ratio	Deflection Error
25	1.120
50	1.060
100	1.030
1000	1.003

$$\textbf{Slenderness Ratio: } \frac{GAL^2}{EI} \tag{73}$$

Where G is the shear elasticity, EI the flexural rigidity, A the cross-sectional area, and L the length of the beam. The amount of error resulting from considering an Euler Bernoulli or Kirchoff's theory rather than Timoshenko or Mindlin-Reissner for a beam or plate, respectively, is shown in Table IV.

Where the deflection error is the ratio between the bending displacement calculated based on the Timoshenko and Euler-Bernoulli assumption, respectively.

The Slenderness ratio of the ReMa X-blade is evaluated as 35467, which results in less than 0.01% of error in the calculated deflection. Within this negligible error, a thin assumption is considered as a valid approximation. Therefore, the ReMa X-blade is considered to be either a thin beam (Euler-Bernoulli) or a thin plate (Kirchoff's theory).

D. Wide Rema Blade

A FEM analysis is performed assuming a wider Rema blade with width $W = 100\,mm$, and shown in Fig. 64.

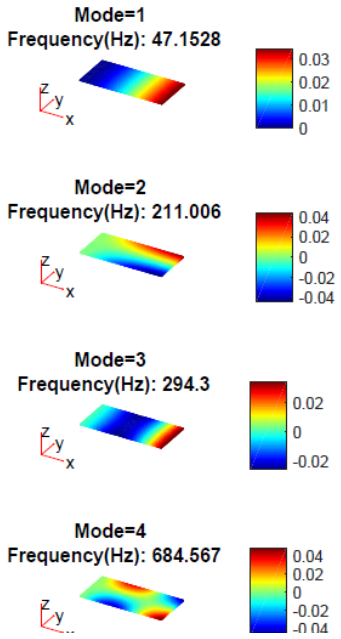

Fig. 64. FEM vibration analysis of a wider rema blade.

It is clear that the beam model is no longer valid where bending and torsional modes combine. Additionally, the con-

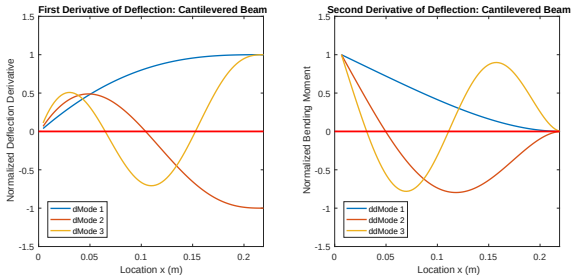

Fig. 65. First and second derivatives of the first three bending mode shapes.

tribution of the vibrations along the width are with considerable modal amplitude relative to the other modes. This is due to the smaller aspect ratio.

E. Optical Placement & Sizing

Based on euler-bernoulli beam model, the first and second derivatives of the first three bending mode shapes are calculated and shown in Fig. 65.

1) Finite Length Analysis: In [1], an analysis of an embedded piezo with finite length was performed based on Hamilton's variational principle. An analytical equation for the electromechanical coupling factor is derived:

$$K_i^2 = \frac{k_{31}^2}{1-k_{31}^2} \frac{c_p^E b_p t_p z_m^2 [\phi_i'(x_2) - \phi_i'(x_1)]^2}{L \mu_i \omega_i^2} \tag{74}$$

Where b_p and L are the piezo width and length, respectively, which is distant z_m from the mid-plane of the beam.

It could be deduced that the piezo length contributes to the coupling factor in two ways:

- The difference of the first derivative of the mode shape (relative rotation) $[\phi_i'(x_2) - \phi_i'(x_1)]^2$ evaluated at the two ends of the piezo patch.
- Inversely proportional length contribution to the coupling factor $\frac{1}{L}$.

Assuming a piezo patch with the first end at the clamp of the beam, the contribution to the coupling factor is visualized in Fig. 9.

In [13], a numerical analysis based on wave propagation was performed which shows that performance is directly proportional to the length up to only 50% coverage of the beam's length. This validates the analytical results reached above, that increasing length doesn't necessarily improve performance. In contrast to what is assumed in some of the literature based on infinitesimal piezo length analysis, which assume that maximum performance is achieved with maximum difference of first derivative of mode shape. These analyses miss the length dependent contribution of capacitance to the coupling factor.

APPENDIX II
VIBRATION DAMPING

A. Passive Damping Robustness

Robustness of passive damping against structural uncertainties can be quantified by perturbing the natural frequency. The passive shunt is tuned for a nominal frequency ω_0, then the damped resonance peak is calculated for the uncertain natural frequency. The robustness analysis is shown in Fig. 66. It could be shown that the damping becomes easily de-tuned such that the performance reaches that of resistive shunting (low) at $0.7\omega_0$ or $1.3\omega_0$ perturbation.

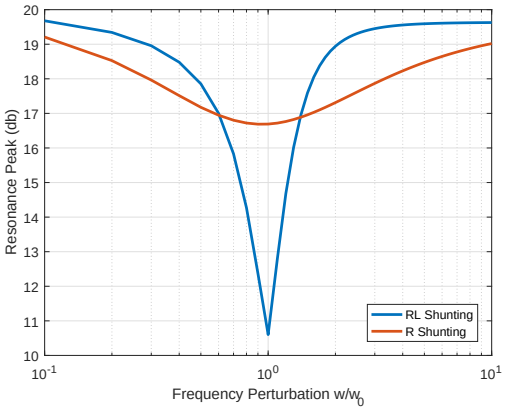

Fig. 66. Robustness of passive RL shunting against perturbing the natural frequency.

APPENDIX III
INSTRUMENTATION & CIRCUITS

In this section, the measurement system and implemented circuitry are presented. Additionally, some evaluation measurements are performed to prove the functionality.

A. Measurement Frame

A frame has been attached to the test-rig in order to mount the optical sensor in front of the blade tip. The setup is shown in Fig. 67. The frame allows for variable height of the optical sensor.

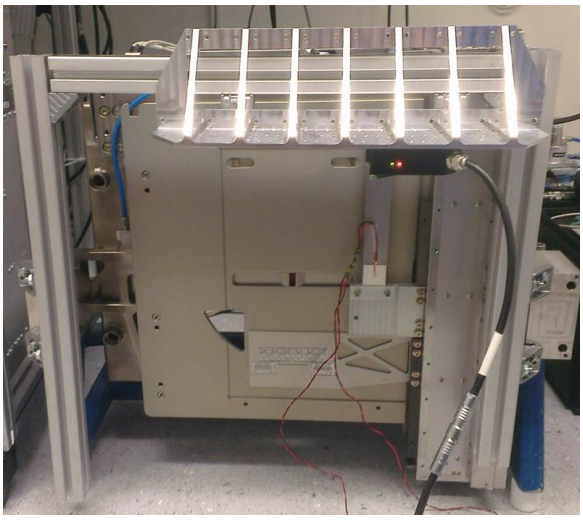

Fig. 67. Frame for mounting the optical sensor.

B. Gyrator Circuit

The gyrator circuit has been implemented using LM324 op-amps as shown in Fig.68.

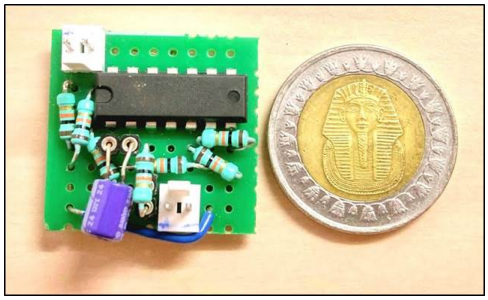

Fig. 68. Comparison inductors versus gyrator.

The following test is performed in order to prove the functionality of the gyrator as a simulated inductor. An RL circuit is formed with the gyrator as shown in Fig.69, where the voltage over the inductor is considered as an output. The input voltage is excited with a sine sweep of $1 - 1.25k\ Hz$. The FRF between the output voltage and input voltage is then estimated. This is compared to the Bode plot of the RL circuit, which forms a high pass filter, and has the following transfer function:

$$G_{RL}(s) = \frac{Ls}{Ls + R_L} \tag{75}$$

Where $R = 10\ k\Omega$, and $L = 700\ H$ are used. The estimated FRF is shown in Fig. 70.

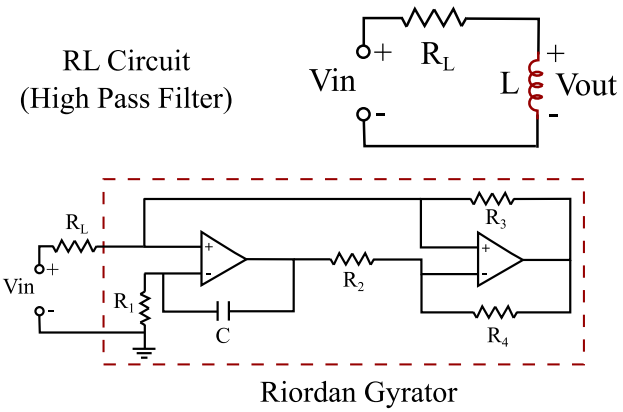

Fig. 69. An RL circuit formed as a high pass filter to test the functionality of the gyrator as a simulated inductor.

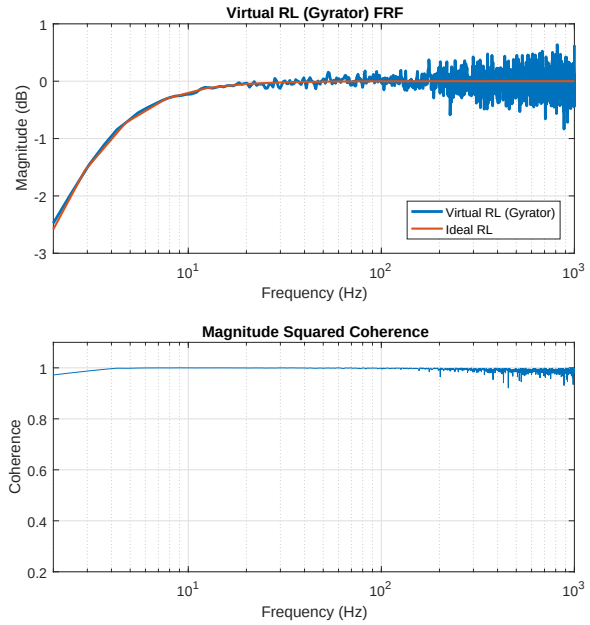

Fig. 70. The FRF of an RL high pass filter formed using the gyrator versus the magnitude Bode plot of the transfer function.

APPENDIX IV
EXPERIMENTAL RESULTS

A. Background Noise

The background noise existing in the Z deflections measurement, without any excitation, is analyzed through the whiteness test. The spectral analysis is shown in Fig. 71. Additionally, the auto-covariance function is evaluated in Fig. 72. In the frequency domain, the noise has a flat spectrum with minor excitation of the blade first and second modes. In the time domain, the auto correlation shows that the signal is uncorrelated. From both analyses, it could be concluded that the background noise is a white signal, hence white noise.

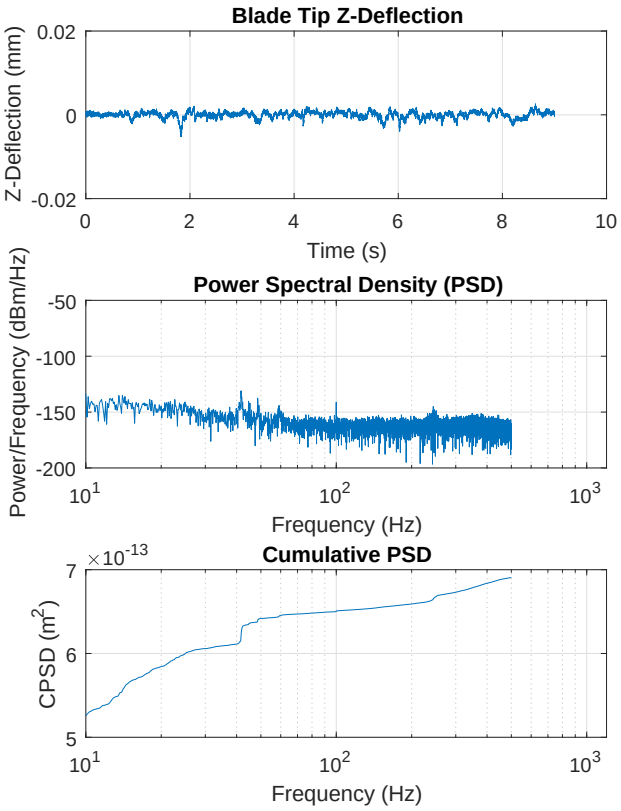

Fig. 71. PSD of background noise shows it has a flat spectrum.

B. Syncing of Measurements (Typical Excitation)

Syncing of different measurements are explained in this section. Syncing is performed based on the uniqueness of the Z profile along the length of the blade. There exists a constant shift of $\approx 1\ mm$ from the tip to clamp of the mover. This constant shift starts at the beginning of the motion, and hence, it could be exactly calculated when does the blade reaches the end position. At the end position, the analysis of settling time of the Z-deflections is started. The time plot of two unsynced measurements is shown in Fig. 73a. Accordingly, the start point of each motion is clearly shown. Compensating for this offset, brings the signals in sync as shown in Fig.'s 73b, and 73c. Finally, zooming into the area of interest yields the analysis plot in Fig. 73d.

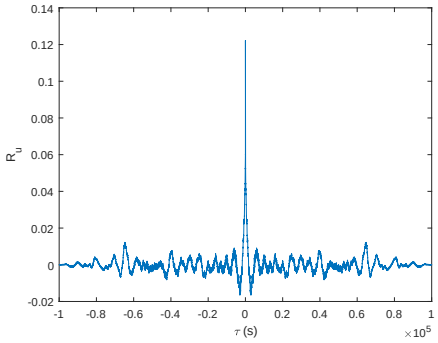

Fig. 72. Autocovariance of the background noise shows that it is uncorrelated.

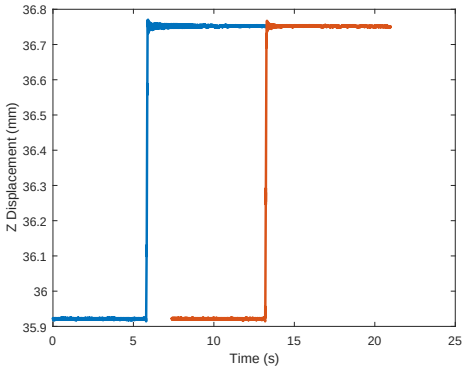

(a) Unsynced Measurements.

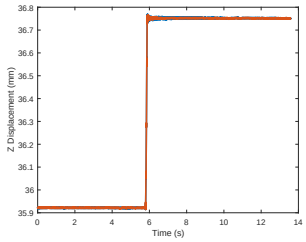

(b) Syncing after offset.

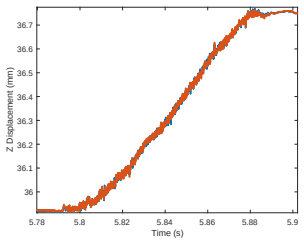

(c) Zoom into start and end points of motion.

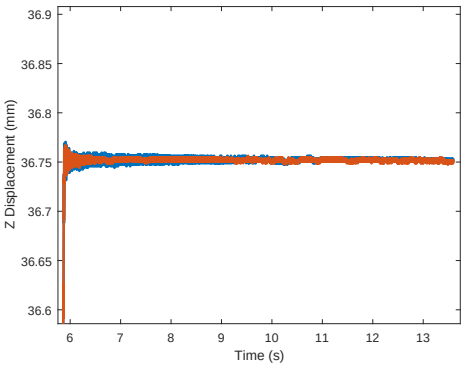

(d) Region of interest.

Fig. 73.

C. x/Fx Transfer

The FRF of the x/Fx transfer is shown in Fig. 74 along with the coherence of the measurement. The FRF is compared to a magnitude Bode plot of $1/ms^2$ with $m = 1.1\ kg$.

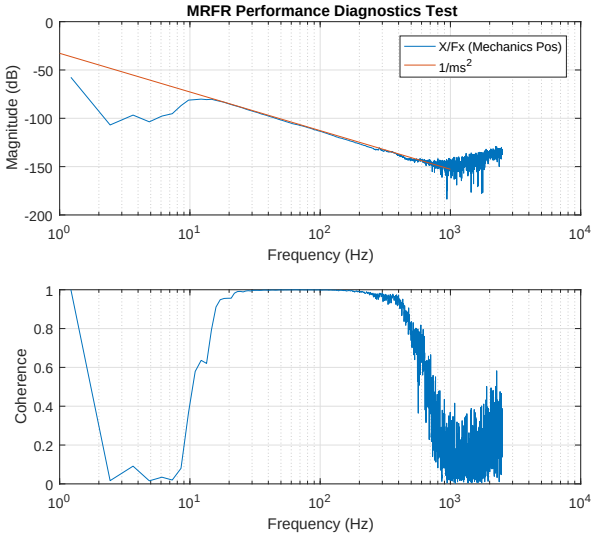

Fig. 74. FRF of the x/Fx transfer with the coherence estimate.

APPENDIX V
MECHANICAL DRAWINGS

A. Blade

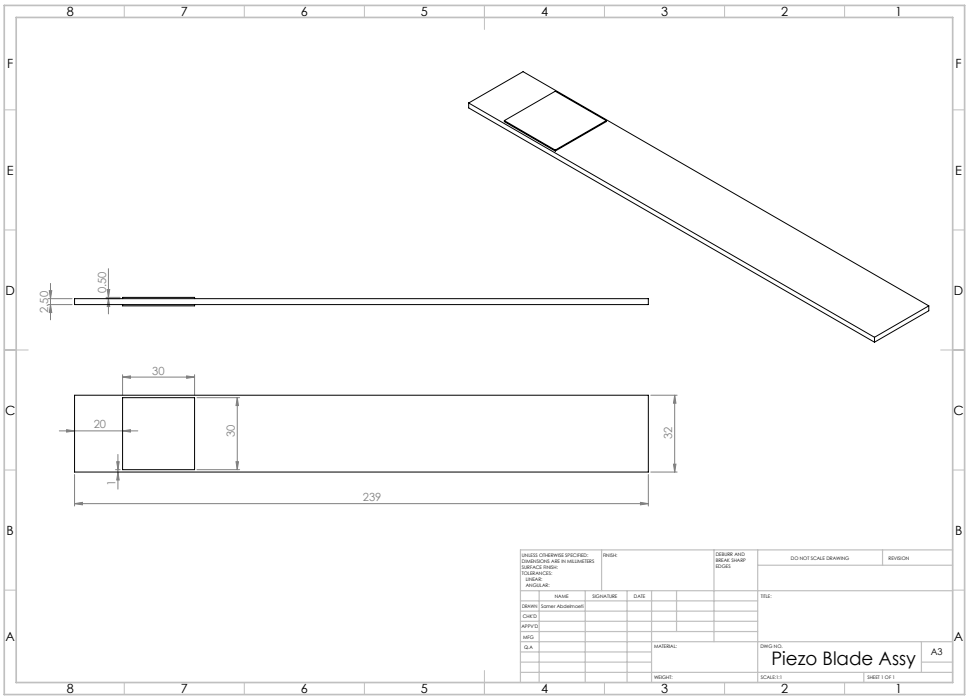

Fig. 75. Piezo embedded into stainless steel blade on both sides.

B. Rema Bracket

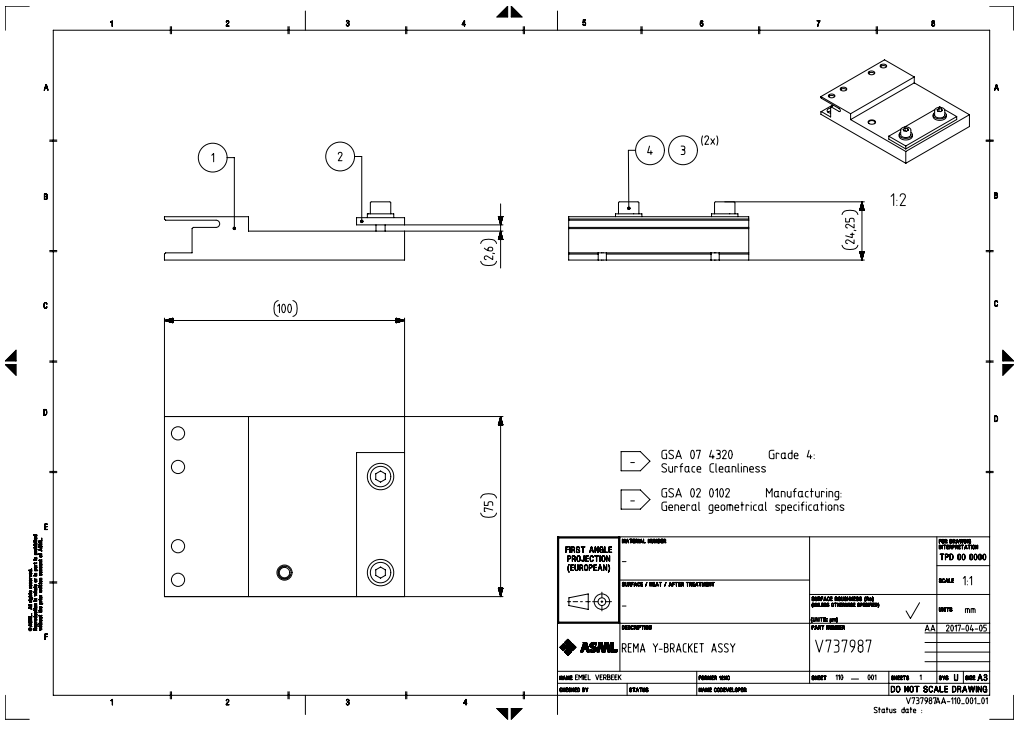

Fig. 76. Bracket attached to the rema test-rig for clamping the blade.

C. Bracket

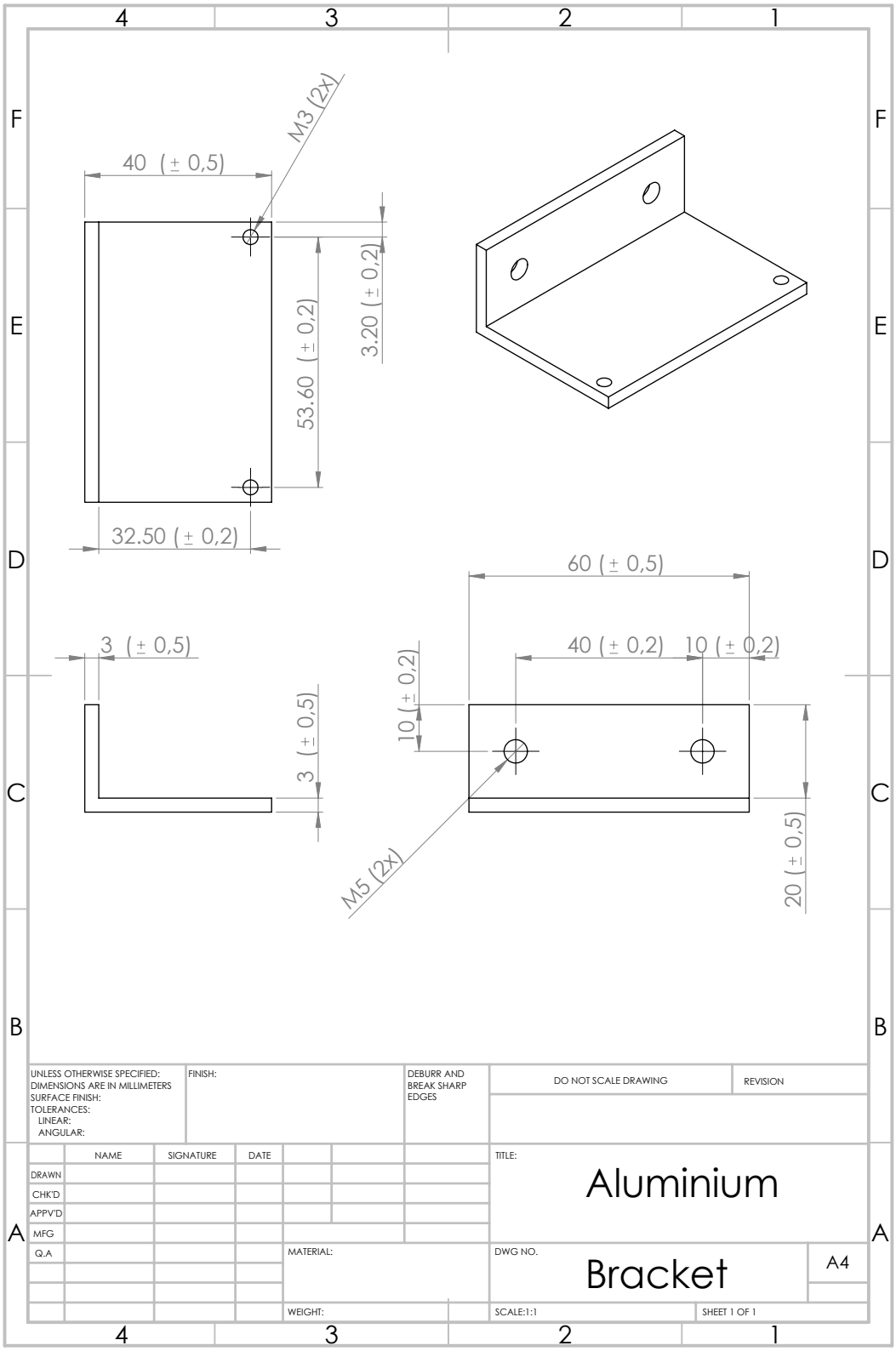

Fig. 77. Bracket attached to the rema bracket to clamp the harvesting piezo.

Conclusions

In this work, a self-powered vibration damping solution has been designed for the vibrating reticle masking blades in a lithography machine. The solution was based on a scanning motion energy harvester for an actively powered damping approach. Firstly, blade vibrations were modeled, analyzed, and identified. Afterwards, piezoelectric patches were embedded on the blade based on optimal placement and sizing analyses. Passive shunting and active feedback controllers were designed for vibration damping. Energy harvesting from the scanning motion was proposed through a cantilevered piezoelectric patch with an appropriate tip mass.

Experimental results show the damping achieved by the powered damping approaches. Dominant mode attenuation of $65\ dbm/Hz$ and $70\ dbm/Hz$ has been achieved for resonant shunting and direct velocity feedback, respectively. Moreover, regulated power output of $2\ mW$ was attained by an energy harvesting circuit. Finally, self-powered vibration damping has been realized by supplying harvested power to the simulated resonant shunt. Vibrations were successfully attentuated with $57\ \%$ of the peak amplitude. Therefore, a standalone solution for vibration damping using piezoelectric materials has been proved feasible through this work.

Recommendations on Vibration Damping using Piezoelectric Materials in High Precision Machines

Samer Abdelmoeti
Email: samer.abdelmoeti@gmail.com

I. Feedforward: Scanning Motion Energy Harvester

Since the vibrations are induced from the scanning motion, a very interesting proposal is to utilize the scanning motion energy harvester as both a feedforward signal and an energy source. Adaptive feedforward filtering [1], could be used to synthesize the filter in between the energy harvester and the single piezo actuator (Fig. 1 to Fig. 2). This should be certain enough to apply feedforward since the scanning motion is precisely controlled. A small current from the raw harvesting piezo output is fed into the filter amplifier. The regulated harvesting piezo DC output powers the amplifiers. The amplifier output is accordingly fed into the actuator piezo, to perform vibration (disturbance) cancellation/compensation.

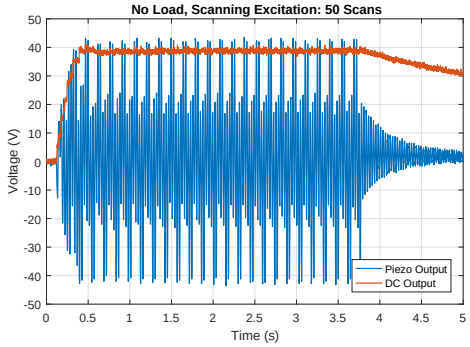

Fig. 1. Harvesting piezoelectric output during scanning.

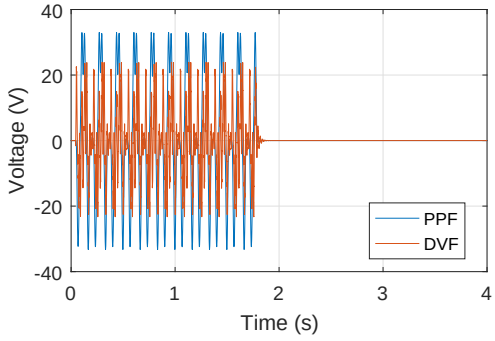

Fig. 2. Control input generated by DVF and PPF to add damping.

II. Measurement setup: Tip Vibrations during Scanning

In this work, an optical sensor was used to measured the vibrations while settling after the excitation. Hence, the damping could be indeed estimated. However, the important quantitative measurement for the specification is to measure the vibrations during the scanning motion. A measurement system which could measure the tip deflections during motion should be design, maybe an accelerometer at the tip. Does the added mass of the accelerometer affect the blade's resonance frequency?

III. Feasibility: Autonomous shunting for higher level vibrations

In other modules, or reticle masking units, the vibrations could be higher than the micro-meter scale. The question is whether autonomous shunting [8] utilizing the vibrations itself would be feasible. The literature proves that it is feasible to provide the amount of power required to switch over an inductor (SSDI) with optimal switching laws, however the performance achieved was less than standrad RL shunting. An important aspect to be analyzed is the power/performance trade-off.

IV. Electronics & Optimization: Active Damping using Op-amps

A limiting aspect in the current configuration is the use of robust high voltage amplifiers (PIVA) in order to drive the low capacitive piezo load. An optimized configuration is to use integrated op-amps with low power consumption that are capable driving the capacitive load. Additionally, PPF should be validated and optimized (H∞-based) experimentally. Moreover, self-sensing actuators could be incorporated.

V. Vibration Damping of Complex Modules

Considering more complex geometry rather than a beam, with analysis on optimal piezo placement and sizing. Is maximum strain location still valid as a compact solution?

The following step in literature is considering a plate (2-D). However, from application point of view, the reticle masking Y-blades could be considered. The first blade has a U-shaped geometry and cantilevered boundary conditions, which makes the analysis more complicated. The other blade has a plate-like geometry with the "narrow" cantilevered boundary conditions.